The Spatiotemporal Evolution of the Diurnal Cycle in Two WRF Simulations of Tropical Cyclones

REBECCA C. EVANS[a] AND DAVID S. NOLAN[a]

[a] *Department of Atmospheric Sciences, Rosenstiel School of Marine and Atmospheric Science, University of Miami, Miami, Florida*

(Manuscript received 12 April 2021, in final form 17 December 2021)

ABSTRACT: The properties of diurnal variability in tropical cyclones (TCs) and the mechanisms behind them remain an intriguing aspect of TC research. This study provides a comprehensive analysis of diurnal variability in two simulations of TCs to explore these mechanisms. One simulation is a well-known Hurricane Nature Run (HNR1), which is a realistic simulation of a TC produced using the Weather Research and Forecasting (WRF) Model. The other simulation is a realistic simulation produced using WRF of Hurricane Florence (2018) using hourly ERA5 data as input. Empirical orthogonal functions and Fourier filtering are used to analyze diurnal variability in the TCs. In both simulations a diurnal squall forms at sunrise in the inner core and propagates radially outward and intensifies until midday. At midday the upper-level outflow strengthens, surface inflow weakens, and the cirrus canopy reaches its maximum height and radial extent. At sunset and overnight, the surface inflow is stronger, and convection inside the RMW peaks. Therefore, two diurnal cycles of convection exist in the TCs with different phases of maxima: eyewall convection at sunset and at night, and rainband convection in the early morning. This study finds that the diurnal pulse in the cirrus canopy is not advectively driven, nor can it be attributed to weaker inertial stability at night; rather, the results indicate direct solar heating as a mechanism for cirrus canopy lifting and enhanced daytime outflow. These results show a strong diurnal modulation of tropical cyclone structure, and are consistent with other recent observational and modeling studies of the TC diurnal cycle.

KEYWORDS: Diurnal effects; Hurricanes/typhoons; Tropical cyclones; Numerical analysis/modeling

1. Introduction

A growing collection of studies have documented how the diurnal cycle in tropical cyclones (TCs) is a significant mode of variability. A comprehensive quantitative evaluation of the spatiotemporal evolution of the diurnal cycle and causal mechanisms in TCs remains elusive, owing to the lack of available observations that can capture the entire TC in adequate resolution in space and time. This study aims to document the primary modes of variability in TCs on the diurnal time scale, and in doing so, evaluate mechanisms behind the responses.

Previous studies have explored observations and simulations of diurnal variability in the areal extent of the cirrus canopy, pulses of upper-level and eyewall deep convection, rainfall, the structure of the secondary circulation, cyclone intensity, and gravity wave radiation. Mechanistically linking the diurnal cycle in cirrus canopy area with diurnal variability in the secondary circulation and eyewall deep convection has been discussed as early as 1977 in observational studies by Browner et al. (1977), Gray and Jacobson (1977), and Muramatsu (1983). These studies attributed diurnal variability in the radial extent of the cirrus canopy to differential heating and cooling of the cloudy and surrounding cloud-free environment inducing an anomalous secondary circulation (Gray and Jacobson 1977). The Gray and Jacobson (1977) differential cooling mechanism was proposed to cause an early morning maximum in tropical convection due to invigoration of convection by the enhanced secondary circulation. Later studies instead attributed diurnal variability to direct interaction of radiation with convection. Randall et al. (1991) found in simulations of deep convection that precipitation varied with both diurnal and semidiurnal frequency, which was attributed to what is now known as the lapse rate mechanism. In this mechanism, upper-level cooling at night increases the local lapse rate, increasing instability, leading to a nocturnal invigoration of deep convection. This was suggested to be the cause for the early morning maximum in precipitation observed over the tropical oceans. Many subsequent studies on the diurnal cycle in TCs have supported direct radiation–convection interaction as a mechanism behind diurnal variability in the cirrus canopy. Kossin (2002) suggested that nocturnal cooling of the cirrus canopy induces subsidence, thereby reducing the area of the cirrus canopy at night in satellite observations.

More recently, new studies have provided a wealth of important insights in to the diurnal cycle in TCs. Dunion et al. (2014) found that in all major North Atlantic hurricanes from 2001 to 2014, a pulse of convection forms near the inner core of the cirrus canopy around the time of local sunset, and propagates radially outward overnight and in to the next day. They proposed multiple mechanisms as a potential cause for the pulse including a trapped convective gravity wave, decreased outflow resistance and inertial stability in the outflow at night, the differential cooling mechanism, and the lapse rate mechanism (Tripoli and Cotton 1989; Mecikalski and Tripoli 1998; Gray and Jacobson 1977; Randall et al. 1991). Additional work on the diurnal pulses by Ditchek et al.

Nolan's current affiliation: Department of Atmospheric Sciences, Rosenstiel School of Marine and Atmospheric Science, University of Miami, Miami, Florida.

Corresponding author: Rebecca C. Evans, rebecca.evans@rsmas.miami.edu

DOI: 10.1175/JAS-D-21-0100.1

(2019a) and Ditchek et al. (2019b) illustrate that these diurnal pulses are ubiquitous throughout the Atlantic Basin hurricane season, and are especially prevalent in major hurricanes, with pulses occurring on 80% of major hurricane days. They mostly occurred when the environmental conditions were more favorable around midnight local time. These diurnal pulses were found to be convectively coupled through association with lightning activity, alluding to the presence of diurnal radially propagating squall lines in a deep-layer below the cirrus canopy of TCs. The diurnal pulses in these observational studies are consistent in finding an outward propagation speed of the cirrus canopy diurnal pulse of 8–14 m s^{-1} (Dunion et al. 2014; Ditchek et al. 2019a).

Simulations and observations of the diurnal cycle in TCs have revealed that the spatiotemporal evolution of diurnal oscillations in TCs are very complex. Tang and Zhang (2016), Tang et al. (2017), and Tang et al. (2019) analyzed simulations of Hurricane Edouard (2014) found an enhancement of nocturnal convection due to the lapse rate mechanism. Furthermore, Tang et al. (2019) illustrated that this peak in convection results in eyewall contraction through increased vertical advection of the tangential wind tendency. Navarro and Hakim (2016) and Navarro et al. (2017) found using idealized simulations that there is a diurnal cycle in temperature, intensity, upper-level outflow, and latent heating in TCs. These signals were found to account for up to 62% of the variance in TC outflow and 28% of variance the boundary layer. They suggest that periodic direct absorption of solar radiation in the cirrus canopy drives an anomalous local overturning circulation in the TC outflow, as shown using a modified version of the Sawyer–Eliassen equations. This result is supported by idealized simulations of TCs by Evans and Nolan (2019) that used diurnal heat forcing derived from realistic simulations. Ruppert and Hohenegger (2018) and Ruppert and O'Neill (2019) found in simulations with nonrotating and TC frameworks that both the lapse rate and differential cooling mechanisms influence the magnitude and phase of the diurnal cycle of precipitation. At night, low- to midlevel convection in the eyewall was found to be invigorated, and surface inflow enhanced. During the day, they found that direct solar heating causes both an anomalous mid- to upper-level secondary circulation, with enhanced upper-level outflow and midlevel inflow, and a lifting of the cirrus canopy. Multiple studies using observations as well as simulations of varying complexity have confirmed that propagating and standing wave responses of diurnal frequency can be supported in the outflow (O'Neill et al. 2017; Evans and Nolan 2019; Knaff et al. 2019). Dunion et al. (2019), using one of the simulations used here (HNR1), found a diurnal squall that forms in the inner core of TCs around sunrise and propagates radially outward. This same sunrise diurnal squall line has been found in lightning, microwave, radar, and infrared observations of Hurricane Harvey (2017) (Ditchek et al. 2020). Knowledge of the diurnal squall is limited, but recent studies find that it appears to follow the diurnal clock of Dunion et al. (2014). The structure of the squall and physical relationship to the cirrus canopy diurnal pulse remain unknown. Zhang et al. (2020) used 2242 GPS dropsondes in 20 mature hurricanes to study the diurnal cycle in boundary layer inflow, finding that the surface inflow is weaker during the day and stronger at night, particularly near the eyewall and outside a radius of 250 km, where in the latter they found the surface inflow to be 2–3 m s^{-1} weaker at local noon.

This study expands on the work of Dunion et al. (2019) by taking an analytical approach to 1) provide a holistic overview of diurnal variability in TCs and 2) evaluate how the diurnally varying cirrus canopy, secondary circulation, convection, and rainband squalls are related to one another. To do so, we use empirical orthogonal functions and Fourier filtering to analyze two high-resolution simulations to provide a detailed spatial analysis of the relative magnitudes and timings of diurnal maxima, in order to discern which of the mechanisms outlined above are the most viable. The first simulation is the Nolan et al. (2013) Hurricane Nature Run (HNR1), which is a well-validated simulation that faithfully captures many observed features of the diurnal cycle (Dunion et al. 2019). The second simulation is a WRF simulation of Hurricane Florence (2018), which is used to assess the robustness of the previous modeling results. As will be described, many of the diurnal oscillations outlined in these previous studies are also present in the simulations performed in this study.

The manuscript is organized as follows. Section 2 outlines the setup of the simulations performed and the analytical methods used. Section 3 presents the main findings by time of day from local sunrise to sunset. Section 4 evaluates the mechanisms that may be responsible for the diurnal variability. Section 5 provides a summary and possible future work.

2. Methodology

To explore spatial variability of the diurnal cycle in TCs, this study uses the azimuthally averaged output from two high-resolution full-physics TC simulations of varying intensity. These are the Nolan et al. (2013) Hurricane Nature Run (HNR1) and a simulation of Hurricane Florence (2018). Both simulations were performed using the Weather Research and Forecasting (WRF) Model with output recorded every 30 min.

a. HNR1

HNR1 is a simulation of the life cycle of a strong TC in the North Atlantic Ocean, which remains far removed from the influence of land for the duration of the simulation (Nolan et al. 2013). It was performed using WRF version 3.2.1, embedded in the Joint Observing System Simulation Experiment (OSSE) global nature run by the European Centre for Medium-Range Weather Forecasts (ECMWF). The outermost WRF domain has 27-km resolution and covers most of the North Atlantic Ocean, within which there are three vortex-following nested grids of 9-, 3-, and 1-km resolution. This study analyzes the output from the 3-km nested domain, since it extends to a large enough radius (360 km) to capture the entire diurnal cycle in the cirrus canopy. Each grid has 61 vertical levels from sea level to 50 hPa. HNR1 uses the RRTM-G radiation scheme to parameterize radiation, the WRF double-moment 6-class scheme for microphysics, and the

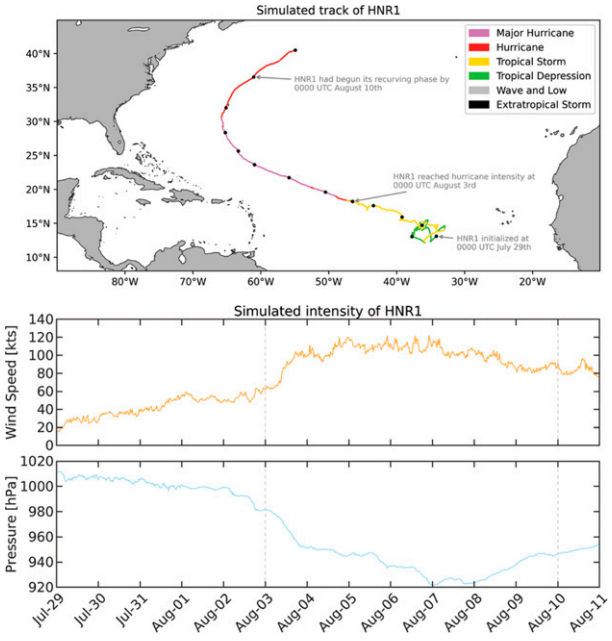

FIG. 1. HNR1 track and intensity. (top) The track and status of HNR1 from the initiation of the simulation at 0000 UTC 29 Jul to the end at 0000 UTC 10 Aug. The black filled circles show the location at 0000 UTC each day. The gray arrows pointing to the locations at 0000 UTC 3 and 10 Aug correspond to the gray dashed lines in the bottom two panels, which delineate the start and end of the part of the HNR1 simulation selected for analysis in this paper (i.e., the period in which the HNR1 TC was at hurricane intensity). Also shown are the time series of the two main intensity metrics: (middle) maximum wind speed (orange) and (bottom) minimum sea level pressure (light blue). The time series tick marks are at 0000 UTC each day.

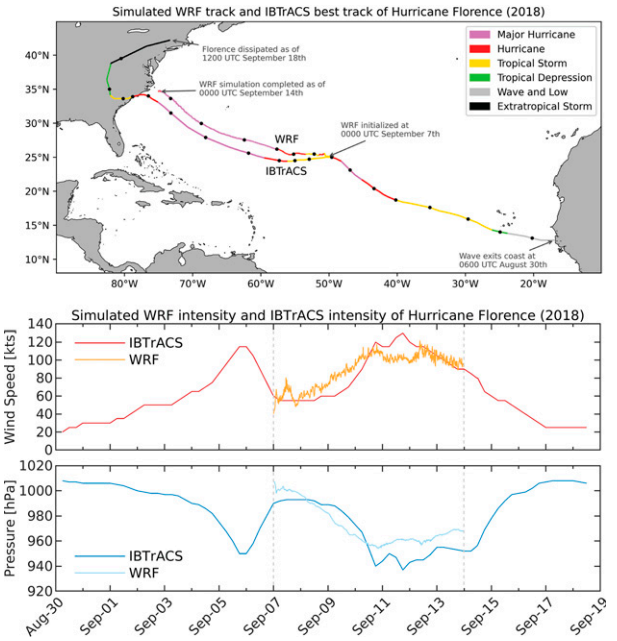

FIG. 2. Florence track and intensity. (top) The track and status of both the real track of Florence from the IBTrACS database, and the track of the WRF-simulated Florence. The gray arrows at 0000 UTC 7 and 14 Sep correspond to the gray dashed lines in the bottom two panels, which delineate the start and end of the WRF simulation. Also shown are the time series of (middle) maximum wind speed and (bottom) minimum sea level pressure of the real Florence (red and dark blue lines) and WRF-simulated Florence (orange and light blue lines). The IBTrACS Florence intensity metrics are plotted every 3 h, and the WRF metrics every 15 min.

Kain–Fritsch scheme (Iacono et al. 2008; Lim and Hong 2010; Kain 2004). The Kain–Fritsch scheme was used on the parent domain and the 9-km nested domain, but not the 3- and 1-km nested domains. The track and intensity of HNR1 is shown in Fig. 1.

b. Hurricane Florence

Hurricane Florence (2018) (hereafter referred to as "Florence") was chosen for this study as it was a real hurricane that resembles HNR1 in track and intensity. Like HNR1, Florence was a long-lasting TC that slowly traversed the Atlantic Ocean with no land interaction, had similar time scales of intensification and weakening, and reached peak intensity at category 4.

Florence formed from a tropical wave near the African coast on 30 August 2018, propagating west-northwestward as a weak disturbance, reaching hurricane intensity on 4 September, undergoing rapid intensification over the next 30 h, followed by a rapid weakening to tropical storm intensity by 0000 UTC 7 September (Stewart and Berg 2019). Thereafter, Florence remained at tropical storm intensity at around 55 kt (1 kt $\approx$ 0.51 m s^{-1}) until 1200 UTC 9 September, after which it underwent a second rapid intensification of 50 kt until 1800 UTC 10 September. Florence reached peak intensity at 130 kt at 1800 UTC 11 September, then slowly weakened on approach to the North Carolina coast, making landfall at 1115 UTC 14 September. From 30 August to 14 September, Florence exhibited two cycles of strengthening and weakening: one from 30 August to 6 September, and one from 7 to 14 September. For this study, the second cycle was chosen to be simulated on the basis that it lay geographically closer to the track of HNR1. The WRF simulation runs for the 7 days from 0000 UTC 7 September to 0000 UTC 14 September. Since the diurnal cycle over land differs in timing from that over the ocean, the WRF simulation ends before Florence makes landfall, so as to remove the mixing of diurnal signals from the land and ocean environments.

Figure 2 shows the real track and intensity of Hurricane Florence (2018) from the International Best Track Archive for Climate Stewardship (IBTrACS) and the simulated track and intensity from WRF. While the WRF track is consistently displaced slightly north of the real track, the intensity aligns very well with the real intensity, with the exception of a slightly earlier onset of rapid intensification, earlier weakening, and faster translation speed from 8 to 13 September. The WRF Florence is not a perfect representation of the real Hurricane Florence, but is a high-quality simulation of a realistic TC using observational/reanalysis data for the initial and

boundary conditions, rendering it a credible simulation with which to compare HNR1.

The Florence simulation was performed using WRF version 4.2.1. Hourly data from the ECMWF ERA5 dataset was used for the initial condition and boundary conditions on the outermost domain (CDS 2017). The outermost domain for the Florence simulation is a 270 × 180 grid with 18-km resolution, covering most of the western Atlantic Ocean, extending from 12° to 41°N and from 85° to 40°W. Within this there are two vortex-following nested grids of 6- and 2-km resolution. The grid sizes for these domains are 180 × 180 and 360 × 360, respectively. The domains were designed so that the innermost high-resolution nest extended to a large enough radius to capture the diurnal cycle, which has been shown in observations to extend beyond radii of 300 km (Dunion et al. 2014). Thus by design, the innermost domain captures the full radial extent of the variability in the secondary circulation. By reproducing the entire diurnal cycle for the TC in high resolution on one domain, we can justifiably show how the diurnal cycles of different variables interact with one another. The 2-km grid spacing in Florence allows a domain with no cumulus parameterization to extend far enough to capture the entire diurnal cycle one grid without the need for a nested grid, and thus without having issues from changes in grid resolution within the domain. A 1-km grid spacing was deemed unnecessary, since it would be prohibitively expensive, with little additional benefit to that provided by the 2-km grid. This grid spacing is low enough to resolve multiple grid points in the diurnal pulses.

All three domains use 61 vertical levels from sea level to 50 hPa (a height of 20 km). The tropospheric vertical levels are similar to those in HNR1: linearly spaced in height from sea level to the top of the boundary layer, then linearly spaced in pressure from the top of the boundary layer to the top of the domain (50 hPa). The vertical levels were defined using a sounding derived from the ERA 5 data at the center of the outermost domain at 0000 UTC 7 September. Florence uses the same parameterization schemes as HNR1, with the exception of cumulus parameterization, for which the updated Tiedtke scheme of Zhang and Wang (2017) was used on the outermost domain, and cumulus parameterization was turned off on both of the nested domains.

To test the sensitivity of the results to microphysics and the height of the domain top, two additional Florence simulations were performed in WRF. One used the Morrison microphysics scheme with the same 20-km domain top described above, and the second used the WRF double-moment 6-class microphysics scheme with a 30-km domain top (Morrison et al. 2009; Lim and Hong 2010). All other parameters remained the same. The vertical grid in the 30-km domain top simulation consisted of 81 levels from sea level to 12 hPa. The vertical level distribution is the same in the troposphere as the 20-km domain top simulation, with the addition of 20 additional levels with 500-m spacing from 20 to 30 km. The 30-km Florence simulation is unique in that it is a high-quality simulation of TC with a higher domain top than is customary. This allows exploration of the interaction of the TC with the lower-stratosphere environment, and removes the possibility of spurious responses in the upper troposphere from the interaction with the upper boundary.

All Florence simulations were initialized with the nested vortex-following domains centered at 25.1°N, 49.8°W, as this was the location of the TC center as of 0300 UTC 7 September 2018 according to the National Hurricane Center advisory 31 for Florence.

c. Analytical methods

In this study, azimuthally averaged output is used for the analysis. The azimuthal averages were computed by interpolating the output on the vortex-following nested grids from polar coordinates in longitude–latitude–height space on to a cylindrical grid. The centers of the cylindrical grids correspond to the center of the vortex-following nests, which in WRF corresponds to the vortex center at 700 hPa. The new vortex position is computed every 15 min. The radial grid spacing of the cylindrical grid was chosen to be the same as the zonal grid spacing at the center of the domain (3 km for HNR1 and 2 km for Florence). The azimuthal grid spacing is 0.36°, such that the azimuthal coordinate is made up of 1000 evenly spaced radial slices. The vertical coordinate is the same as that of the polar grid. The data are interpolated from the domain output in polar coordinates to this cylindrical grid, and a mean taken in the azimuthal dimension to produce the azimuthal means.

Fourier filtering and empirical orthogonal function analysis (EOFs) were used to quantitatively evaluate modes of variability in the azimuthally averaged output. The Fourier filtering was used to show explicitly diurnal variability in space and time. The EOFs were used to show the modes of variability that are close to diurnal in nature, and the variances explained by these diurnal modes. All of the results were computed in UTC, but plotted in local time (LT) so the results could be interpreted relative to the local diurnal cycle. For the Fourier and EOF analysis of HNR1, only the output from 0000 UTC 3 August to 0000 UTC 10 August was used, while the TC was at hurricane intensity. For the same analysis of Florence, only the output from 0000 UTC 8 September to 0000 UTC 13 September was used, to remove the first day when it was at tropical storm intensity and the last day when it was approaching land. Removal of the days when the TCs are weak prevents spurious center locations, and thus invalid azimuthal averages, from being incorporated in to the analysis dataset.

To perform the Fourier filtering, a time series of a given variable was taken at each grid point of the azimuthally averaged data in radius–height (r–z) space. A Fast Fourier Transform was performed on that time series, the corresponding amplitudes for all frequencies not equal to 1 day^{-1} were set to zero, then the Fourier Transform was inverted. This yielded r–z fields spatiotemporally filtered for the diurnal cycle. Note that the amplitudes corresponding to the diurnal frequency are slightly lower than they likely are in reality, since 30 min temporal resolution is too low to completely isolate amplitudes corresponding to the many harmonics of the diurnal frequency (i.e., some of the power corresponding to 1 day^{-1} projects on to other frequencies). Previous work has shown

that solar forcing projects on to higher frequencies than the diurnal component due to rapid changes in heating rate at sunrise and sunset, meaning that diurnal modulation goes beyond responses on the diurnal time scale (O'Neill et al. 2017; Evans and Nolan 2019). However, this study will primarily focus on oscillations with exactly diurnal frequency.

To perform the EOF analysis, the data were detrended to prevent the long-term intensification and weakening of the TCs projecting on to the EOFs. To achieve this, a time series of a given variable was taken at each grid point in the azimuthally averaged r–z fields, and the 24 h centered moving mean was removed from that time series to yield the anomalous fields. The moving average is truncated at the edges of the analysis period, and does not exploit excluded time steps in the calculation. The EOF analysis was then performed on the anomalous fields for each variable, and the principal component (PC) time series were rescaled such that the PC time series maximized at 1. The spatial map was rescaled accordingly, by multiplying all points in r–z space by the maximum value of the PC time series. To evaluate to what extent a given PC time series illustrates a diurnal mode, the PC time series was Fourier filtered for the diurnal frequency, and the time of the daily peak calculated from the diurnally filtered PC time series. In this study, only EOFs with a visibly present diurnal component to the PC time series will be shown.

3. Results

The results will be presented by the time of day to provide an overview of the progression of changes in the average day of a TC, grouped by the average local times of sunrise, solar noon (hereafter "midday"), and sunset in the simulation. For the sake of this discussion, sunrise, midday, and sunset are defined as the first recorded time in the day when the storm-averaged shortwave heating rate is greater than zero, the time of the shortwave heating daily maximum, and the last recorded time in the day when shortwave heating is greater than zero. In HNR1, the average local times of sunrise, midday, and sunset are 0530, 1230, and 1900 LT, respectively. In Florence, the average local times of sunrise, midday, and sunset are 0600, 1230, and 1830 LT, respectively.

Figure 3 provides context of the primary modes of variability for shortwave (SW) and longwave (LW) radiation in both HNR1 and Florence. The first leading EOFs (EOF1) for SW heating in Figs. 3a and 3d explain more than 99.5% of the variance, and are representative of the typical spatial pattern and temporal evolution of SW heating in a TC. The PC time series depicts the archetypal truncated sinusoid of diurnal SW heating. The optically opaque cirrus canopy dominates the absorption of SW radiation, and thus exhibits the strongest diurnal cycle of SW heating in the TC with an amplitude of up to 0.5 K h^{-1}. The eyewall SW heating diurnal cycle is comparatively much weaker, with an amplitude of up to 0.12 K h^{-1}. EOFs 1 and 2 for LW in Figs. 3b, 3c, 3e, and 3f show the increase in upper cirrus canopy LW emission just prior to solar noon, while the lower cirrus canopy is strongly heated by LW radiation emitted from the clouds below. LW EOF's 1 and 2 in HNR1 and Florence represent radiation emission responses to the upward and downward displacement of the cirrus canopy throughout the day, and vertical thickening and thinning of the cirrus canopy near the inner core in the late afternoon to early evening. These responses will be discussed in more detail in subsequent sections.

On the whole, the results presented below indicate that HNR1 and Florence both show prominent diurnal variability that are very consistent with other studies. Florence exhibits weaker diurnal variability than HNR1. This is likely a consequence of three main factors: first, Florence occurred later in the year when the diurnal cycle of solar radiation is itself weaker; second, Florence was a weaker storm for a greater proportion of its life cycle than HNR1; last, Florence was more asymmetric than HNR1, meaning some variability was smoothed out in the azimuthal-averaging process. While diurnal variability in Florence is generally weaker, the spatial patterns and phases of diurnal variability are very consistent with HNR1. In both simulations, a diurnal squall forms around sunrise, the cirrus canopy moves upward at midday, the outflow is enhanced at midday, and eyewall convection reaches peak intensity at sunset.

a. Sunrise

Around sunrise in both HNR1 and Florence, the prominent diurnal feature is a squall that forms just outside the inner core (around 2–3 times the radius of maximum wind) before sunrise and propagates radially outward throughout the day, reaching peak intensity just after sunrise. Previous studies using observations have suggested that this squall line is vertically deep, and appears to approximately follow the diurnal clock of Dunion et al. (2014) in timing, radial location, and propagation speed (Dunion et al. 2019; Ditchek et al. 2020).

EOFs for which the PC time series peaks around sunrise in HNR1 (0530 LT) are shown in Fig. 4. Figures 4a and 4b illustrate that reflectivity (dBZ) has two prominent diurnal modes owing to the presence of a radially propagating diurnal squall, as in Dunion et al. (2019) who first noted this phenomenon in HNR1. This is a column-deep squall line that forms just outside the inner core just before sunrise, as shown in 4a, and propagates outward over the course of the day, as shown in 4b. EOF2 for dBZ peaks at 0330 LT, at which time there is an anomalously high dBZ from r = 150–200 km. This is the radial location at which the squall forms just before sunrise. Thereafter, the squall propagates outward, amplifying in intensity as it does so. By 0830 LT, at the peak of EOF1 in Fig. 4b, the squall reaches its peak intensity at r = 200–220 km. In Fig. 4c, the unfiltered PC time series for equivalent potential temperature (θ_e) is a relatively smooth sinusoidal wave of diurnal frequency. The unfiltered PC time series is extremely similar to the diurnally filtered PC time series which peaks at 0600 LT each day, 30 min after sunrise. The spatial pattern shows a number of important features, including a negative anomaly of 1–3 K in the cloud-free eye and tropopause. A weak positive θ_e exists in the cloudy eyewall, cirrus canopy, and rainbands of the TC. There is a large positive θ_e anomaly of up to 5 K in the boundary layer at r = 200–300 km, representative of a strong humidification of the boundary layer in this location at sunrise.

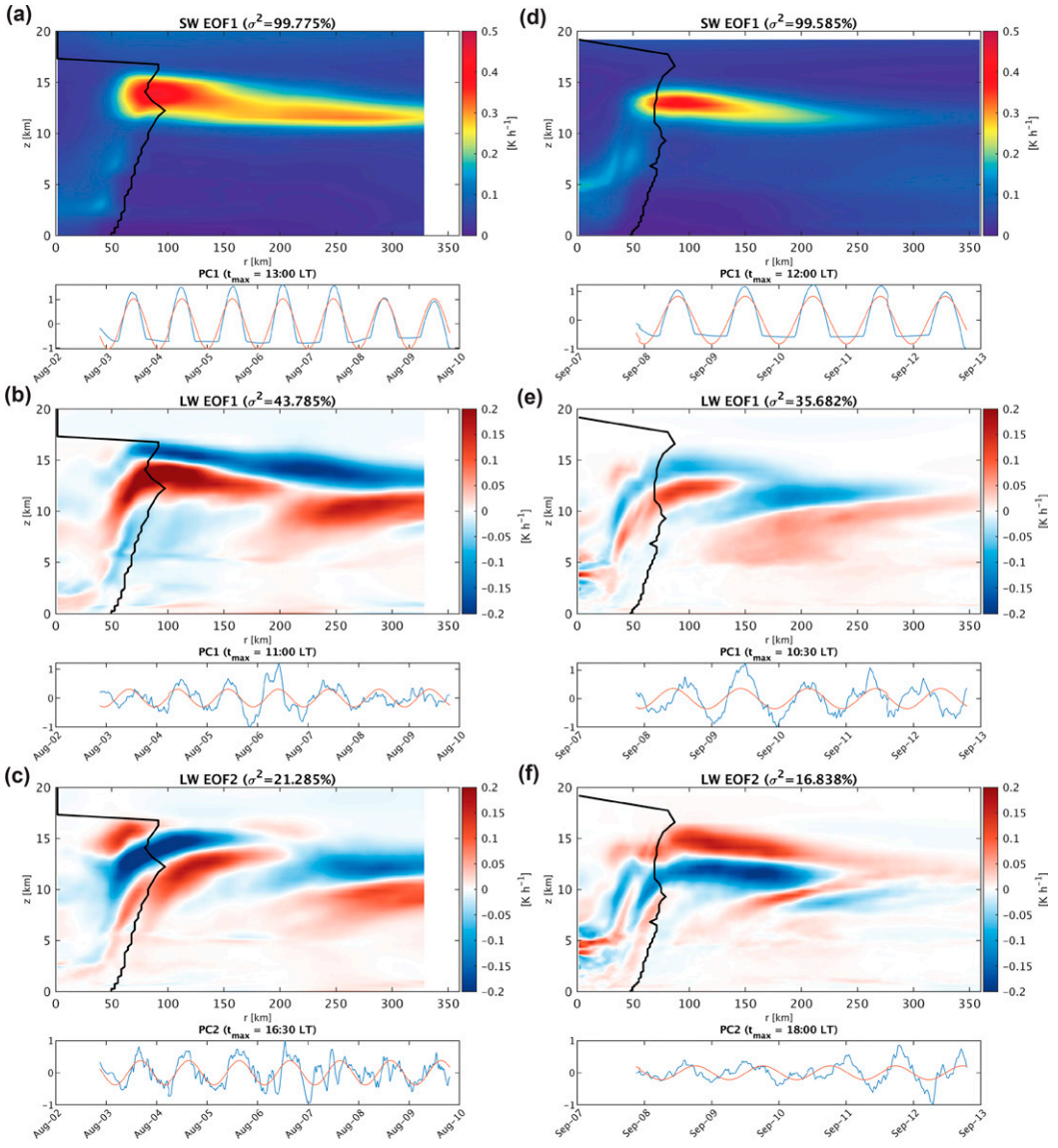

FIG. 3. EOFs for uncoupled SW and LW radiation. (left) HNR1 (a) SW EOF1, (b) LW EOF1, and (c) LW EOF2. (right) Florence (d) SW EOF1, (e) LW EOF1, and (f) LW EOF2. For each EOF, the r–z spatial pattern is shown in the top panel, and the PC time series in the bottom panel. In the spatial pattern, the black line shows the average position of the RMW. In the PC time series, the blue line shows the original unfiltered PC time series, and the red line shows the diurnally filtered PC time series. The percentage of the variance explained by the EOF (σ^2) and the local time at which the diurnally filtered PC time series peaks (t_{max}) are shown in parentheses above the spatial pattern and PC time series, respectively. Note that the HNR1 panels are shown out to r = 360 km to aid comparison with Florence. All times in this and subsequent figures are in local time, with tick marks in the time series at 0000 LT each day.

This humidification is coincident with the passage of the diurnal squall, which will be discussed more later in this section. The squall appears to reach its maximum intensity just prior to the maximum θ_e and also in surface water vapor fluxes in this location (not shown), implying that these signals are a consequence of the passage of the squall. It is possible this could provide positive feedback on the squall line, or enable the rehumidification of the environment after the passage of the squall line. Further properties of the diurnal squall in HNR1 will be discussed later in this section. EOF1 for dBZ explains more variability since it captures the amplification of the pulse at larger radii.

The same diurnal squall is present in Florence around sunrise (0600 LT) as shown in Fig. 5. As before, the squall forms at inner radii before sunrise, and propagates outward throughout the day, reaching peak intensity just after sunrise.

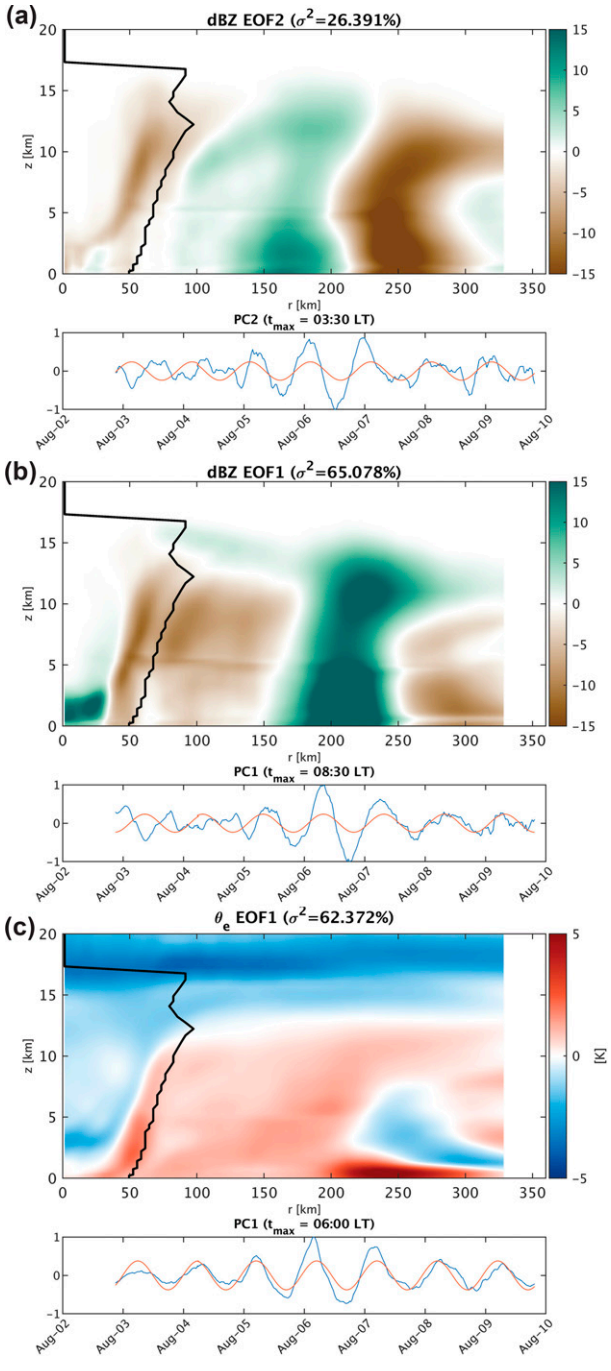

FIG. 4. Sunrise EOFs for HNR1: (a) dBZ EOF2, (b) dBZ EOF1, and (c) θ_e EOF1.

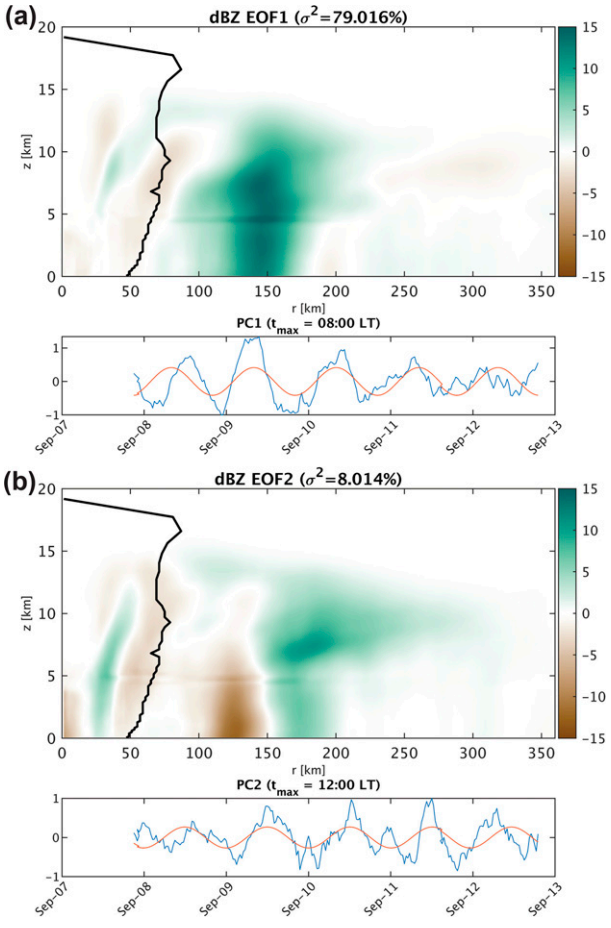

FIG. 5. Sunrise EOFs for Florence: (a) dBZ EOF1 and (b) dBZ EOF2.

EOFs 1 and 2 for dBZ illustrated that in the simulated Florence, the primary mode variability is the amplification of rainband rainfall just after sunrise (Fig. 5a), and the secondary mode of variability is radial propagation from around r = 125–180 km (Fig. 5b). The squall reaches its peak maximum intensity at r = 150 km by 0800 LT, at the peak of the PC time series in EOF1 (Fig. 5a). After reaching peak intensity, the squall continues to propagate outward and weakens. The PC time series for both EOF1 and EOF2 of dBZ in Florence are less smoothly diurnal than those in HNR1, as the diurnal variability in Florence is in general weaker than in HNR1.

To illustrate the propagation characteristics of the diurnal squalls in both HNR1 and Florence, Hovmöller diagrams of rain mixing ratio (Q_{rain}) are shown in Fig. 6. Figures 6a and 6d show Hovmöller diagrams of the unfiltered Q_{rain} at around 4 km height. This height was chosen since it is where the EOFs for Q_{rain} have the largest amplitude oscillations (not shown). To explore the diurnal oscillations of Q_{rain} at each radius, the Hovmöller diagrams in Figs. 6a and 6d were Fourier filtered for the diurnal frequency, producing the Hovmöller diagrams in Figs. 6b and 6e. Figures 6c and 6f are the same as Figs. 6b and 6e, but zoomed in to an individual day to show the times of formation and propagation speed more easily. The magenta lines in Figs. 6c and 6f show the approximate position of the cirrus canopy diurnal pulse from Dunion et al. (2014) for context of the relative timing, location, and propagation speed of the diurnal squall. The Fourier filtering was performed on the full date ranges

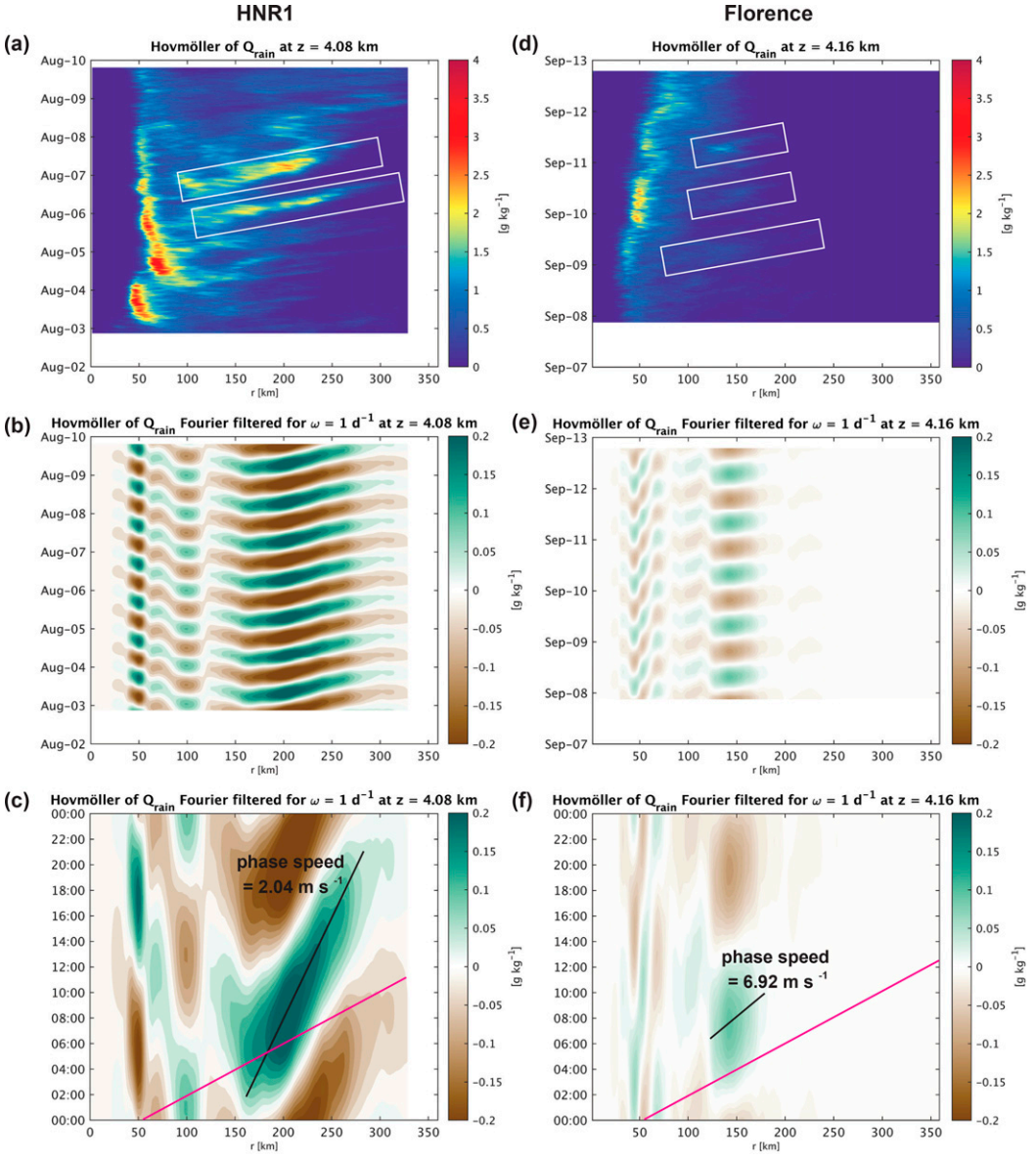

FIG. 6. Hovmöller diagrams of unfiltered and filtered Q_{rain} in (a)–(c) HNR1 and (d)–(f) Florence. (a),(d) The unfiltered Q_{rain} at the level closest to 4 km height. The white boxes in (a) show the propagation of the diurnal squalls when HNR1 was near peak intensity. The white boxes in (d) show the extremely weak diurnal squalls in Florence. (b),(e) Q_{rain} at the same heights filtered for the diurnal cycle. (c),(f) As in (b) and (e), but zoomed in to an individual day. The black lines in (c) and (f) illustrate the propagation speed of the squall. The magenta lines show the approximate radial location at any given time of diurnal pulses in the cirrus canopy based on the diurnal clock in Fig. 10 of Dunion et al. (2014). All times shown are in local time.

shown in Figs. 6a and 6d, as opposed to applying the filter to intervals of a few days when the squall lines were most discernible. This was to allow filtering of the maximum possible length of time series, increasing the fidelity of the result. As such, the filtering includes days of weaker variability, meaning that while the propagation speed and timing of the filtered squall matches that of the unfiltered squall, the exact magnitude of its amplification is weaker than that of the unfiltered squall lines.

In the unfiltered Hovmöller diagrams of Q_{rain} for HNR1 (Fig. 6a), the propagation of the diurnal squall is most obvious for the 2 days when the TC is at peak intensity, as shown in the white boxes. In the filtered Hovmöller diagrams of Q_{rain} in Fig. 6b, multiple propagating features are evident. One originates at r = 100 km and propagates inward to just inside the average radius of maximum wind (RMW), which is at r = 60 km at z = 4 km. The other is the diurnal squall, which first becomes evident at r = 160 km and propagates outward.

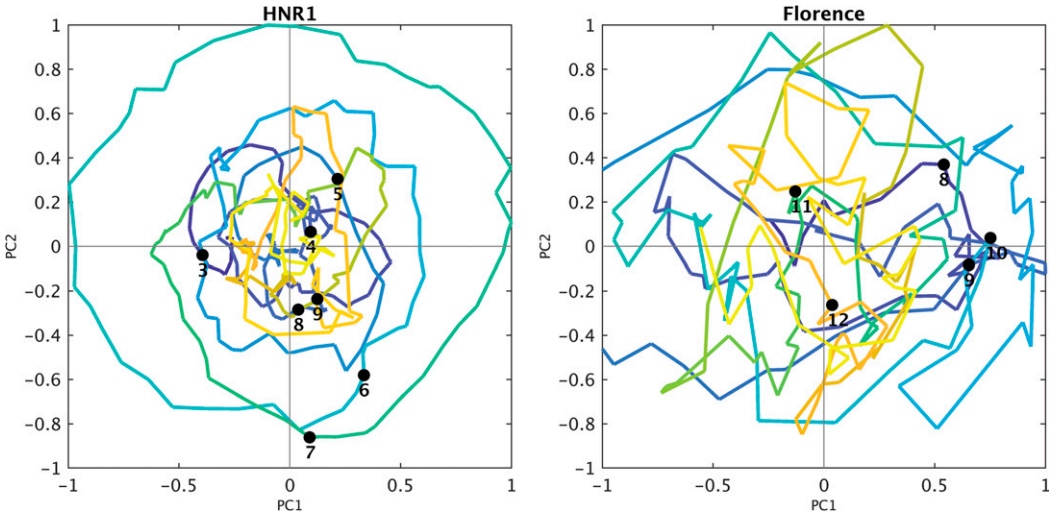

FIG. 7. Phase space points for dBZ for (left) HNR1 and (right) Florence. These plots show the blue lines in Figs. 4a and 4b, and Figs. 5a and 5b plotted against one another. The darkest blue shows the principle components at the start of each simulation, which evenly grade to bright yellow at the end of the simulations. The black dots denote 0000 LT on the dates indicated by the corresponding numbers. The line for HNR1 can be followed in a clockwise direction from the starting point.

The intensification and translation speed of the diurnal squall are more evident in Fig. 6c. The propagation speed of the diurnal squall was estimated by drawing an approximate best fit line through the positive Q_{rain} anomaly outside $r = 160$ km. From this estimate, the diurnal squall in HNR1 appears to propagate radially outward at 2.04 m s^{-1} (3.97 kt). As the diurnal squall propagates outward it intensifies, reaching peak intensity at $r = 200$ km around 0800 LT, just after sunrise. This intensity is maintained for a few hours then the squall begins after to weaken after midday as it continues to propagate outward. The squall dissipates at the edge of the domain at $r = 325$ km. As evident in Fig. 6c, the diurnal squall in Florence appears to propagate more slowly than the cirrus canopy diurnal pulse.

In the unfiltered Hovmöller diagrams of Q_{rain} for Florence (Fig. 6d), the diurnal squall is much less obvious than in HNR1. However, after Fourier filtering for the diurnal cycle, the diurnal squall is evident as shown in Fig. 6e. Like in HNR1, inside $r = 125$ km, there are multiple radiating features, some which propagate inward and some which propagated outward. Since Florence is a radially smaller TC than HNR1, the diurnal rainband squall forms at an inner radius compared to that of HNR1. In Florence, the squall forms at $r = 120$ km and only propagates outward to 180 km, whereas in HNR1 the squall forms near $r = 150$ km and propagates outward to beyond $r = 300$ km. Additionally, the Florence squall propagates faster than in HNR1 and intensifies less than in HNR1. However, while the diurnal squall in Florence is much weaker, its propagation speed is remarkably similar to that of the diurnal pulse in the cirrus canopy. The propagation speed of the squall in Florence is 6.94 m s^{-1} (19.3 kt). This propagation speed varied among the Florence simulations performed here, and will be discussed further in section 3d. Despite the difference in squall propagation speed and intensity between Florence and HNR1, the timing of the formation and intensification of the squall is the same in both simulations. The squall in HNR1 propagates substantially slower than the diurnal pulse in Dunion et al. (2014) and Ditchek et al. (2019a).

The propagation of the squall lines in HNR1 and Florence are shown in Fig. 7 using phase space points for dBZ. As shown in Fig. 7a, the radial propagation of the diurnal pulse in HNR1 is clearly evident through the circular nature of the plot. The larger circles represent the days when the diurnal squall was most apparent (6 and 7 August). As shown in Fig. 7b, evidence of radial propagation of the diurnal squall in Florence is essentially absent. Thus, the squall line appears to be present, but not propagate very far if at all. To further explore why the radial propagation diurnal squall in Florence is so different to that of HNR1, we examined the non-azimuthally averaged rain mixing ratio as shown in Fig. 8. This illustrates that (i) the simulated Florence is rather asymmetrical, and (ii) the rainband squall is indeed fairly static throughout the day. Instead of a propagating signal, the diurnal squall appears to manifest in Florence as a daytime amplification and nighttime weakening of rainband convection, which remains at approximately the same radius throughout the day. The rainband convection is disparate in the early morning then appears to amplify just after sunrise, in agreement with the results for HNR1. However, as the day progresses in to the early afternoon, the rain becomes weaker and more asymmetrical, meaning by the rain signal is smoothed out by the azimuthal averaging. In both HNR1 and Florence, the squall appears to form at a large enough radial distance from the eyewall where the downdrafts from the eyewall are less limiting on moisture availability for the squall line. It may be the case that in larger storms like HNR1, the squall line can then propagate outward, but in smaller storms like Florence,

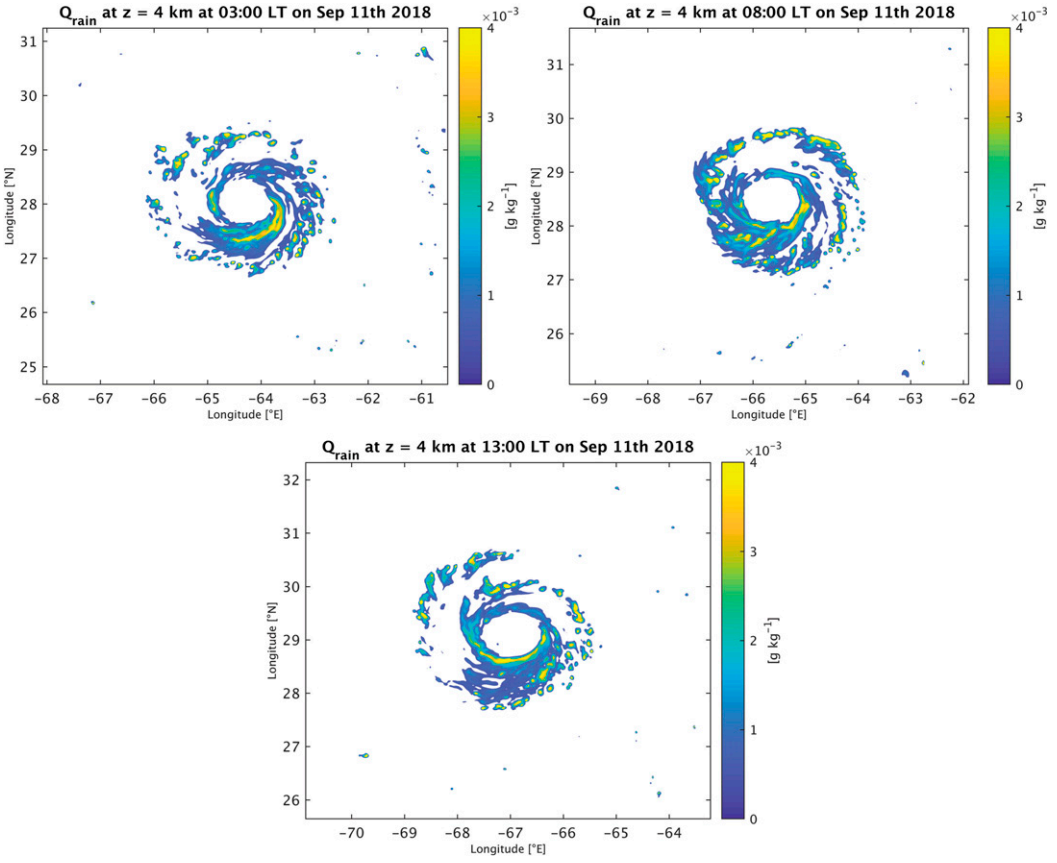

FIG. 8. The squall line in Florence at (top left) 0300, (top right) 0800, and (bottom) 1300 LT 11 Sep 2018. Note that the convection is disparate in the morning and becomes heavily asymmetrical by the afternoon.

the extent to which this is possible is reduced. In both HNR1 and Florence, we find that diurnal oscillations in inertial stability are very weak in the radial range in which the squall would propagate, so we deem this unlikely to be the cause of the discrepancy between HNR1 and Florence. This will be discussed more in section 4.

b. Midday

Around midday in both HNR1 and Florence, the predominant diurnal features are the enhancement of the upper-level outflow, weakening of the surface inflow, and the lifting of the cirrus canopy.

EOFs for which the PC time series peaks around midday in HNR1 (1230 LT) are shown in Fig. 9. For all the EOFs shown in Fig. 9, the diurnal cycle dominates the signal as evident by the unfiltered PC time series oscillating in a smooth diurnal sinusoid much like the filtered time series. Figure 9a shows that most of the variance in radial wind (56.7%) is explained by a diurnal oscillation in surface inflow, midlevel radial wind, and upper-level outflow. At midday, the upper-level outflow is stronger by 4–6 m s^{-1}, in the middle levels the flow is anomalously inward by 1–3 m s^{-1}, and the surface inflow at r = 150–250 km is weaker by around 3 m s^{-1}. This surface inflow weakening is likely a consequence of two factors. First, by local noon, the diurnal squall has propagated very slightly beyond this radial range, and thus relative to r = 150–250 km the inflow into the squall would be in the radially outward direction. This in turn could be related to a positive anomaly in the upper-level outflow. Second, we find in both simulations that direct radiative heating of the upper levels enhances the mid- to upper-level secondary circulation, and through balanced dynamics, this could cause a weakening of the radial flow at the surface. At midnight, this pattern would be the opposite, with much weaker upper-level outflow and stronger surface inflow. This two-layered diurnal oscillation in the overturning circulation is consistent in magnitude and timing with the modeling studies of Ruppert and Hohenegger (2018) and Ruppert and O'Neill (2019). The oscillation in surface inflow is also remarkably consistent in magnitude, timing, and radial location with observations of boundary layer winds in Zhang et al. (2020). The stronger surface wind speeds overnight may be causing the surface humidification through enhancing the evaporation from the ocean surface, accordingly causing the θ_e signal in Fig. 4a. As will be discussed later, the diurnal oscillation in tangential wind in this location is negligible, implying that the diurnal variability in total wind speed in this location is dominated by that of the inflow. As such, a diurnal oscillation in wind speed of up to 3 m s^{-1}

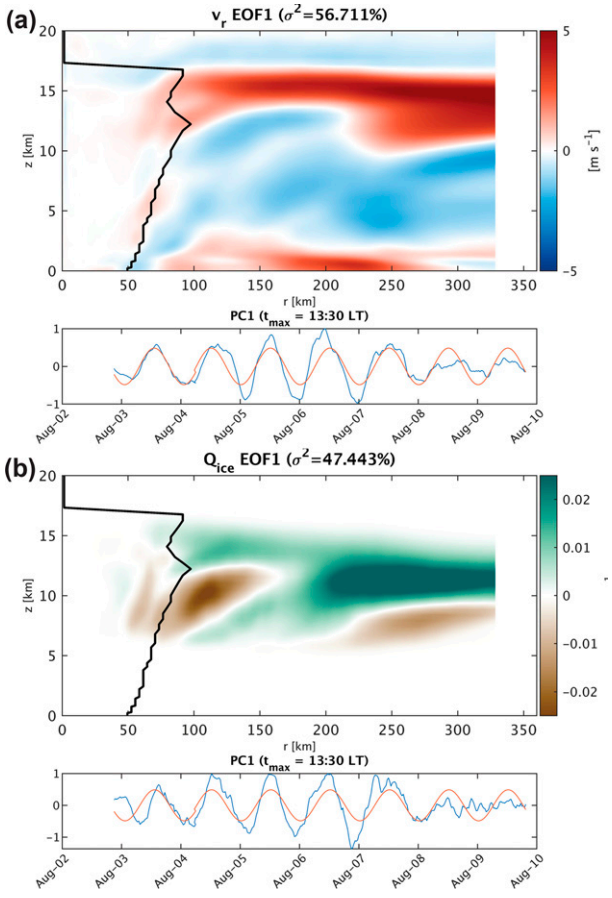

FIG. 9. Midday EOFs for HNR1: (a) v_r EOF1 and (b) Q_{ice} EOF1.

would be enough to cause a change in surface fluxes. Figure 9b shows that 47.4% of the variance in ice mixing ratio (Q_{ice}) is explained by a diurnal oscillation in the height of the cirrus canopy. The spatial pattern for Q_{ice} EOF1 shows an increase in Q_{ice} at midday at the top of the cirrus canopy, and a decrease in Q_{ice} at the bottom of the cirrus canopy. This indicates an upward vertical displacement of the cirrus canopy at midday, as will be discussed in more detail below.

EOFs for which the PC time series peaks around midday in Florence (1230 LT) are shown in Fig. 10. The midday EOFs are largely the same as in HNR1, with a two-layered response in v_r, and an oscillation in the height of the cirrus canopy. In Fig. 10a, EOF1 for v_r is extremely similar to that of HNR1, especially the spatial pattern in the mid- to upper levels and the variance explained by that mode. While the spatial pattern of EOF1 for v_r in Florence is the same as in HNR1, the positive anomaly in the upper-level outflow in Florence is around half of that in HNR1. The positive anomaly in the surface inflow is much weaker than in HNR1 and at a smaller radius. The negative anomaly in midlevel v_r is relatively strong compared to the positive anomaly in the upper-level outflow. While in HNR1 the negative anomaly in the midlevels was half the magnitude of that in the upper-level outflow, in Florence they are comparable. This suggests that the anomalous overturning circulation in the mid- to upper levels dominates the v_r response in Florence, while in HNR1 the two layers of the anomalous overturning circulation (low- to midlevels, and mid- to upper levels) are more comparable. However, for the most part, the responses are the same with respect to the spatial pattern and timing. Therefore, for both HNR1 and Florence most of the variance in v_r is explained by a two-layered response that smoothly oscillates with a diurnal period, as evident by the close match of the unfiltered principal component time series with the diurnally filtered time series. In Fig. 10b, EOF2 for v_r (not shown for HNR1) shows that in the late afternoon, the surface inflow is anomalously weak. It is possible that the weaker surface inflow seen in v_r EOF1 in HNR1 is being represented in Florence in v_r EOF2. In Fig. 10c, EOF1 for Q_{ice} illustrates that the primary mode of cirrus canopy ice variability in Florence is a midday enhancement in the amount of ice and nighttime reduction. The negative Q_{ice} anomaly that was seen in the lower cirrus canopy in Fig. 9c is largely absent. However, in Fig. 10d, showing EOF2 for Q_{ice}, this negative anomaly in the lower cirrus canopy returns, but only at radii less than 200 km. Outside r = 200 km, the negative anomaly is absent altogether. This implies that inside 200 km the cirrus canopy lifts up during the day and subsides at night, while outside the 200 km the cirrus canopy does not move up and down throughout the day, but rather is created and destroyed. During the day at radii beyond 200 km, ice forms leading to areal expansion of the cirrus canopy, while at night Q_{ice} decreases to a point where the cirrus canopy is no longer deemed to be present. EOF2 for Q_{ice} is more similar to that of EOF1 in HNR1. This suggests that in Florence, EOF1 shows the daytime increase in the amount of ice, and EOF2 shows both the diurnal oscillation in the height of the cirrus canopy inside r = 200 km and the creation and destruction of the cirrus canopy outside r = 200 km. In Fig. 10e, EOF1 for Q_{vapor} shows a midday reduction in moisture inside r = 200 km, while overnight there is an increase in moisture, suggesting a more favorable environment for convection overnight.

To explore how the diurnal cycle in the height of the cirrus canopy varies by radius in both HNR1 and Florence, Hovmöller diagrams of cirrus canopy height are shown in Figs. 11a and 11c. For the purposes of this study, the height of the top of the cirrus canopy was defined on the basis of what would be detectable in satellite imagery. Here we define the top of the cirrus canopy as the point at which total precipitable water (TPW) integrated downward from the top of the domain crosses the threshold value of 12 mm, since this is the minimum TPW at which the *GOES-16* Advanced Baseline Imager band 4 (daytime cirrus band) can detect ice (Schmit et al. 2018). The calculation of TPW was performed using the azimuthally averaged Q_{ice} output. To explore the diurnal oscillations of cirrus canopy height at each radius, the Hovmöller diagrams in Figs. 11a and 11c were Fourier filtered for the diurnal frequency, and the amplitude and phase of the diurnal cycle at each radius plotted in Figs. 11b and 11d.

In HNR1 (Fig. 11a), the height of the top of the cirrus canopy is 14–15 km in the inner core, sloping down to around 11.5 km at the edge of the domain. Since the HNR1 TC is large, the cirrus canopy extends beyond the edge of the

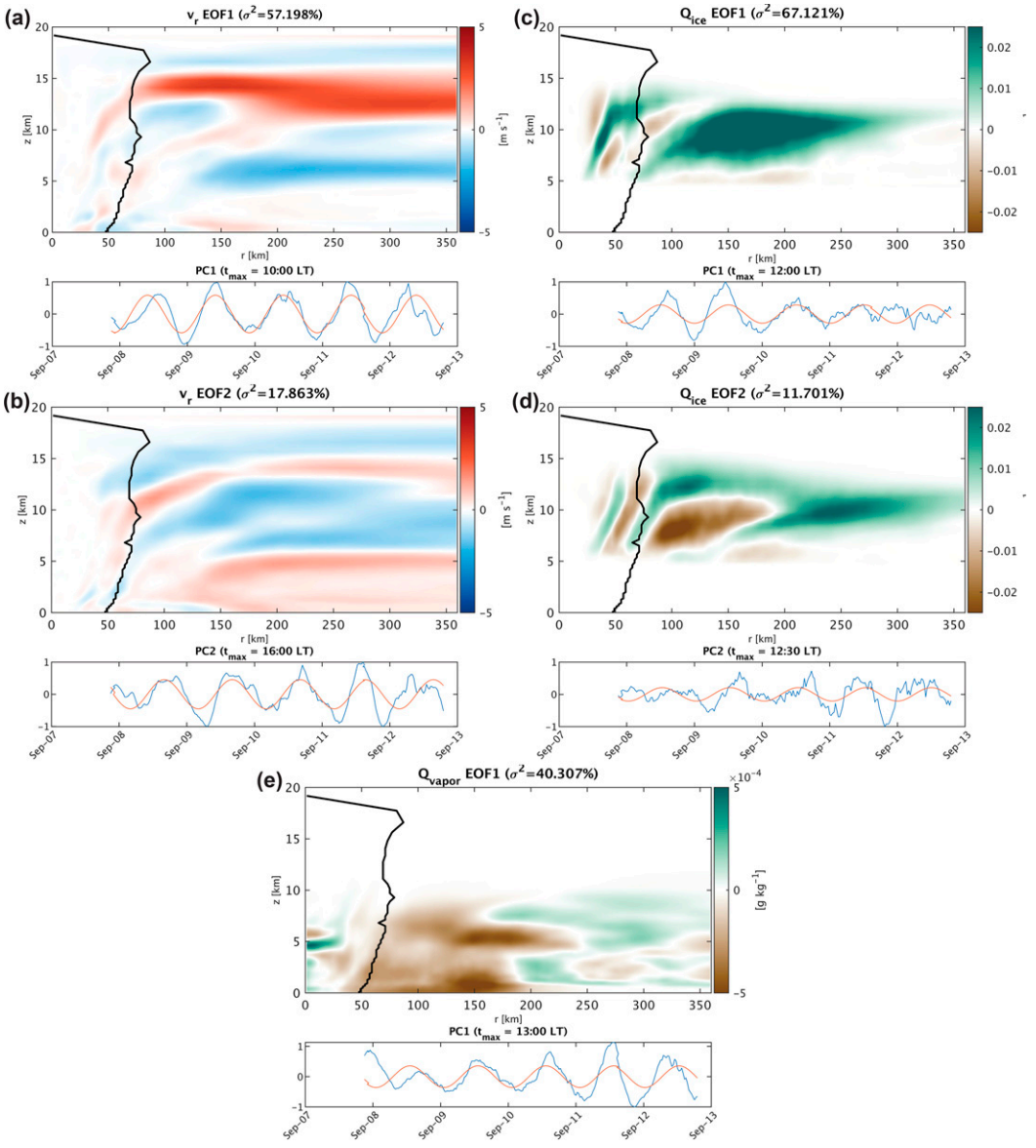

FIG. 10. Midday EOFs for Florence: (a) v_r EOF1, (b) v_r EOF2, (c) Q_{ice} EOF1, (d) Q_{ice} EOF2, and (e) Q_{vapor} EOF1.

domain, so any diurnal oscillation in cirrus canopy area would not be captured in the domain setup used. In HNR1, the entire cirrus canopy is displaced diurnally with an amplitude of 0.2–0.5 km (Fig. 11b). The entire cirrus canopy reaches its maximum altitude around midday, between 1000 and 1400 LT. Since the phase of the maximum height does not increase linearly with radius, this suggests that the oscillation in cirrus canopy height is not a horizontally advective feature (i.e., the enhanced outflow at midday possibly advecting ice from smaller radii where the cirrus canopy is consistently higher does not cause the increase in cirrus canopy height at outer radii). Instead, the entire cirrus canopy appears to rise by around the same amount seemingly in unison. This is likely due to thermally direct lifting as suggested in Ruppert and O'Neill (2019), where midday solar heating lifts the cirrus canopy.

In Florence (Fig. 11c), the cirrus canopy is lower everywhere than in HNR1, with a maximum height of 13 km in the inner core, sloping down to 9–10 km in the outer radii. Since Florence is smaller and the innermost domain extends further, the domain captures the entirety of the cirrus canopy, meaning the diurnal oscillation in cirrus canopy area is evident. At night, the radial extent of the cirrus canopy is around 80 km less than during the day. Accordingly, since for much of the domain (outside r = 200 km) the cirrus canopy is not present overnight, the amplitude and phase of the diurnal cycle of cirrus canopy height are not computed at these radii since the time series are incomplete. At the radii where the cirrus canopy is consistently present, the cirrus canopy from r = 65–100 km oscillates in height with a relatively low amplitude of 0.2 km. Beyond r = 150 km, on approach to the periphery of the cirrus canopy,

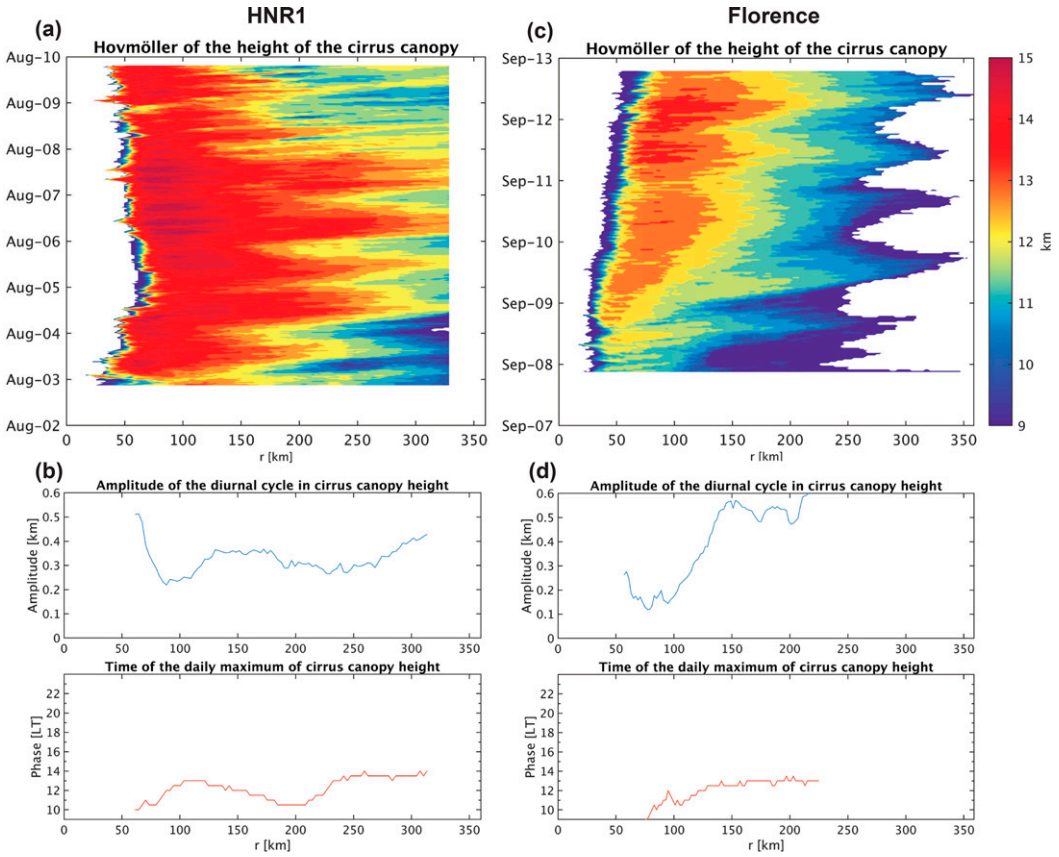

FIG. 11. The height of the top of the cirrus canopy in (a),(b) HNR1 and (c),(d) Florence. (a),(c) Hovmöller diagrams of the cirrus canopy height. (b),(d) The amplitude and phase of the diurnal cycle in cirrus canopy height at a given radius. Amplitude and phase are only shown for radii where the cirrus canopy is present for the entire time span at which the respective TC is at hurricane intensity.

the amplitude of the height oscillation increases substantially to 0.5 km. In the inner core and outer radii, the phase is very consistent with HNR1, with the cirrus canopy reaches maximum height around midday.

As in HNR1, for Florence the cirrus canopy appears to rise simultaneously at all radii, suggesting it is not a horizontally advective response. In HNR1 and Florence, respectively, the maximum daily v_r in the outflow is 12 and 15 m s^{-1}. At this speed, even if ice were advected at the same speed as the outflow, it would take 4–5 h for ice to be advected from the inner core to the outer radii. Since the entire cirrus canopy moves up and down virtually simultaneously, it seems unlikely that the underlying mechanism behind diurnal oscillations in cirrus canopy area is horizontal advection of ice, but instead due to thermally direct lifting. The diurnal oscillation in the height of the cirrus canopy is consistent with the results of with Ruppert and Hohenegger (2018) and Ruppert and O'Neill (2019).

c. Sunset

Around sunset, the diurnal features are not consistent between HNR1 and Florence. Indeed they appear to be in diametric opposition to one another.

EOFs for which the PC time series peaks around sunset in HNR1 (1830 LT) are shown in Fig. 12. In Fig. 12a, EOF1 for tangential wind (v_t) shows that 60% of the variance in v_t is explained by a relatively smooth diurnal oscillation of the winds in the entire wind field. At sunset, v_t is anomalously positive by up to 7 m s^{-1} near the surface just inside the RMW. Elsewhere, winds in the eyewall are stronger by 3–4 m s^{-1} and in the remaining inner core wind field the winds are stronger by up to 2.5 m s^{-1}. In the outermost outflow, v_t is weaker by 1 m s^{-1}. Near the surface, from r = 120–220 km and z = 1–3 km, v_t is weaker at sunset, since the positive v_t anomaly in this location occurs 12 h earlier at sunrise as a result of the diurnal squall. In Fig. 12b, the moist convective heating (MCH) EOF1 spatial pattern is reflective of the eyewall moving radially in and out over the day, and convection outside the RMW in the rainbands. The PC time series is less convincingly diurnal than most others, perhaps due to the high-frequency variability of convection. While the TC is at peak intensity, from 5 to 8 August, the diurnal component to the PC time series is clearer, implying that a diurnal contraction and expansion of the eye is more prevalent in stronger TCs. This sunset–nighttime contraction of the eye is in agreement with the results of Tang et al. (2019). The eyewall contraction

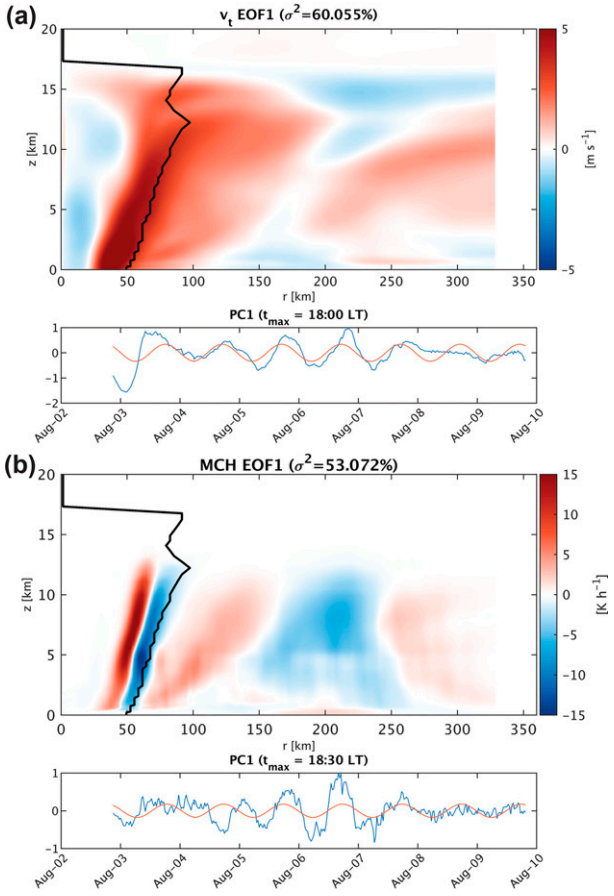

FIG. 12. Sunset EOFs for HNR1: (a) v_t EOF1 and (b) MCH EOF1.

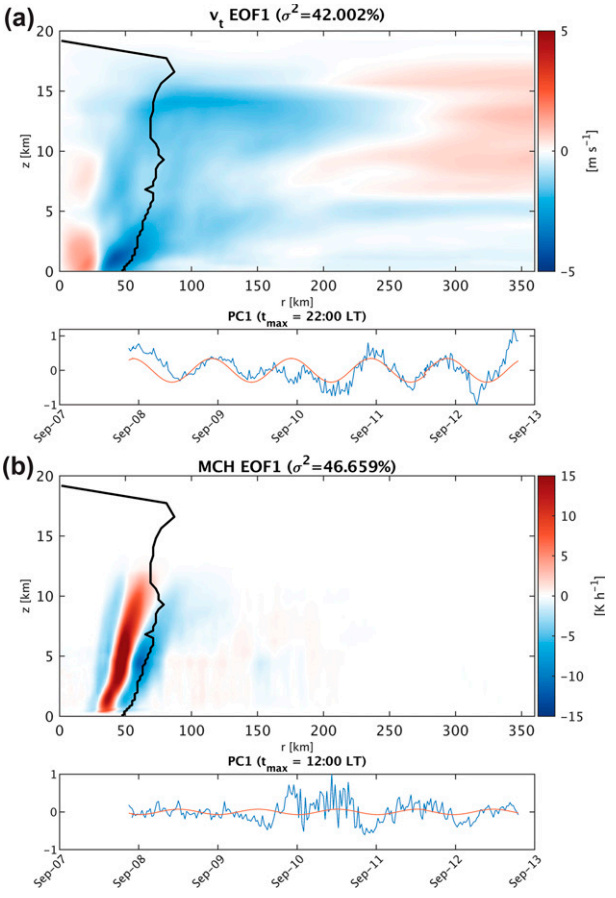

FIG. 13. Sunset EOFs for Florence: (a) v_t EOF1 and (b) v_t EOF2.

in combination with the increase in v_t at sunset indicates an intensification of the TC at sunset, and a sunset peak in eyewall convection. This sunset peak in eyewall convection is supported by the filtered Hovmöller of Q_{rain} for HNR1 in Fig. 6c, where a diurnal peak in eyewall rainfall occurs between 1600 and 2200 LT at a radius of 50 km. This indicates that two convective regimes exist within a TC that vary diurnally with different phase: the rainband squall which forms in the early morning and peaks in the late morning to midday, and the eyewall which peaks in the later afternoon through sunset. Although not shown here, EOF3 for MCH illustrates a weakly diurnal oscillation in the thickness of the eyewall, with a thicker eyewall in the late afternoon.

EOFs for which the PC time series peaks around sunset in Florence (1900 LT) are shown in Fig. 13. In Fig. 13a, EOF1 for v_t shows that 42.0% of the variance in v_t is caused by essentially the opposite mode as in HNR1. In Florence at sunset the v_t anomaly in most of the wind field is negative by up to 2 m s^{-1} instead of positive like in HNR1. The PC time series peaks at 2200 LT with a value of 0.25. Accounting for this value, the maximum diurnal strengthening and weakening of v_t is around 0.5 m s^{-1}. An oscillation of this magnitude is inconsequential when compared to diurnal oscillations of other components of the TC, such as those outlined in the previous sections. In Fig. 13b, EOF1 for MCH is more similar in spatial pattern to EOF1 for MCH in HNR1 with the exception of the PC time series having almost no diurnal component to it at all. EOF1 for MCH instead illustrated more high-frequency variability. None of the EOFs for MCH in Florence exhibit a strongly diurnal mode, suggesting that for Florence, diurnal modulation of eyewall convection is largely insignificant.

d. Sensitivity simulations

To test the influence of the domain setup and microphysics on the Florence simulation, two additional Florence simulations were performed in WRF. One used the Morrison microphysics scheme (Morrison et al. 2009) with the same 20-km domain top described above, and the second used WRF double-moment 6-class as in the simulation above (Lim and Hong 2010) but with a 30-km domain top.

Some of the results of the sensitivity simulations are shown in Fig. 14. EOF1 for v_r in both the Morrison scheme simulation and the 30-km domain top simulation are very consistent with the results of both HNR1 and the Florence simulation outlined above (Figs. 14a,c). There is a midday enhancement of upper-level outflow and anomalous midlevel inflow. In the Morrison scheme the v_r response is top heavy, with a strong

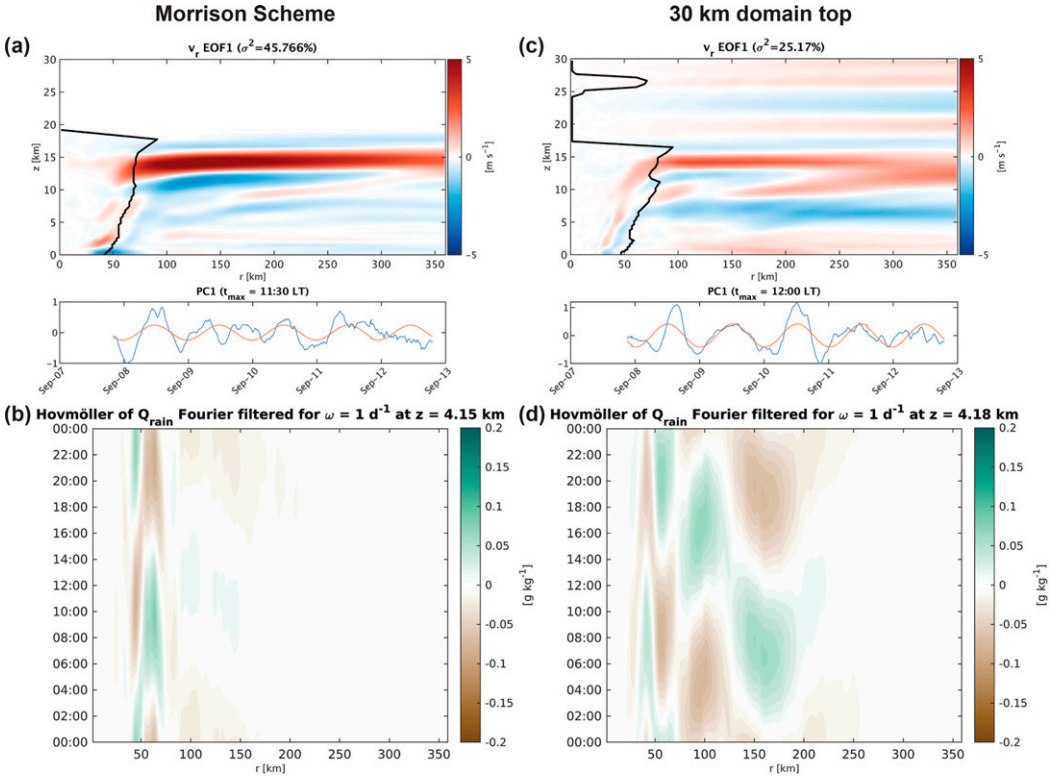

FIG. 14. The sensitivity simulations for Florence. (a),(b) The simulation with the 20-km domain top using the Morrison scheme. (c),(d) The simulation with the WRF double-moment 6-class scheme and a 30-km domain top. (a) v_r EOF1 for Morrison scheme Florence, (b) one day of the diurnally filtered Hovmöller diagram of Q_{ice} as in Fig. 6f for Morrison scheme Florence, (c) v_r EOF1 for 30-km domain top Florence, and (d) one day of the diurnally filtered Hovmöller diagram of Q_{ice} as in Fig. 6f for 30-km domain top Florence. Note that the vertical axis in (a) has been extended to 30 km to aid comparison with (b).

overturning circulation above 10-km height, and no significant oscillation in surface inflow. Whereas in the 30-km domain top simulation, response is more like the two-layered response seen in HNR1 is more evident, with an anomalously weak surface inflow at midday. The v_r responses in both simulation match the spatial pattern, timing, and exhibit the same smooth diurnal oscillation as in the HNR1 and Florence simulations outlined above.

The diurnal squall is more inconsistent between simulations as shown in Figs. 14b and 14d. While in the simulations outlined above, the diurnal squall forms at radii of 120–150 km and propagated outward over the next few hours, in the sensitivity simulations the diurnal squall does not appear to propagate outward. In the Morrison scheme simulation, the rainband squall does not appear to be significantly present. In both the Morrison scheme simulation and the WRF 6-class double moment scheme, EOF1 for Q_{rain} (not shown) illustrates that the diurnal squall is uniformly weak at all vertical levels up to the 5 km melting level, and does not appear to significantly propagate. Whereas in the 30-km domain top simulation, there is a squall which appears to simply amplify and weaken in place at $r = 160$ km. The poor representation of the diurnal squall is present in many other sensitivity simulations that are not shown here, especially those performed the newest version of WRF (version 4.2.1). One simulation performed using an older version (version 3.9.1.1) captured the diurnal squall more reliably, but other variables much less so. The majority of the results presented here are consistent with other studies using both modeling and observations.

e. Synopsis of results

Holistic overviews of the diurnal cycle in HNR1 and Florence are provided in Figs. 15–18.

Figure 15 illustrates the diurnal cycle in the primary and secondary circulation of HNR1. The left panels show the amplitude corresponding to a frequency of 1 day^{-1} (the diurnal cycle), and the right panels show the time at which the daily maximum value occurs (phase). The amplitude and phase are computed using Fourier filtering as described in section 2c. In the phase plots, the pale yellow corresponds to the average local time of sunrise in the simulation, the red is midday, the purple is sunset, and the black overnight. The phase is only shown where the amplitude is ≥1% of the maximum amplitude. As shown in Figs. 15a and 15b, at

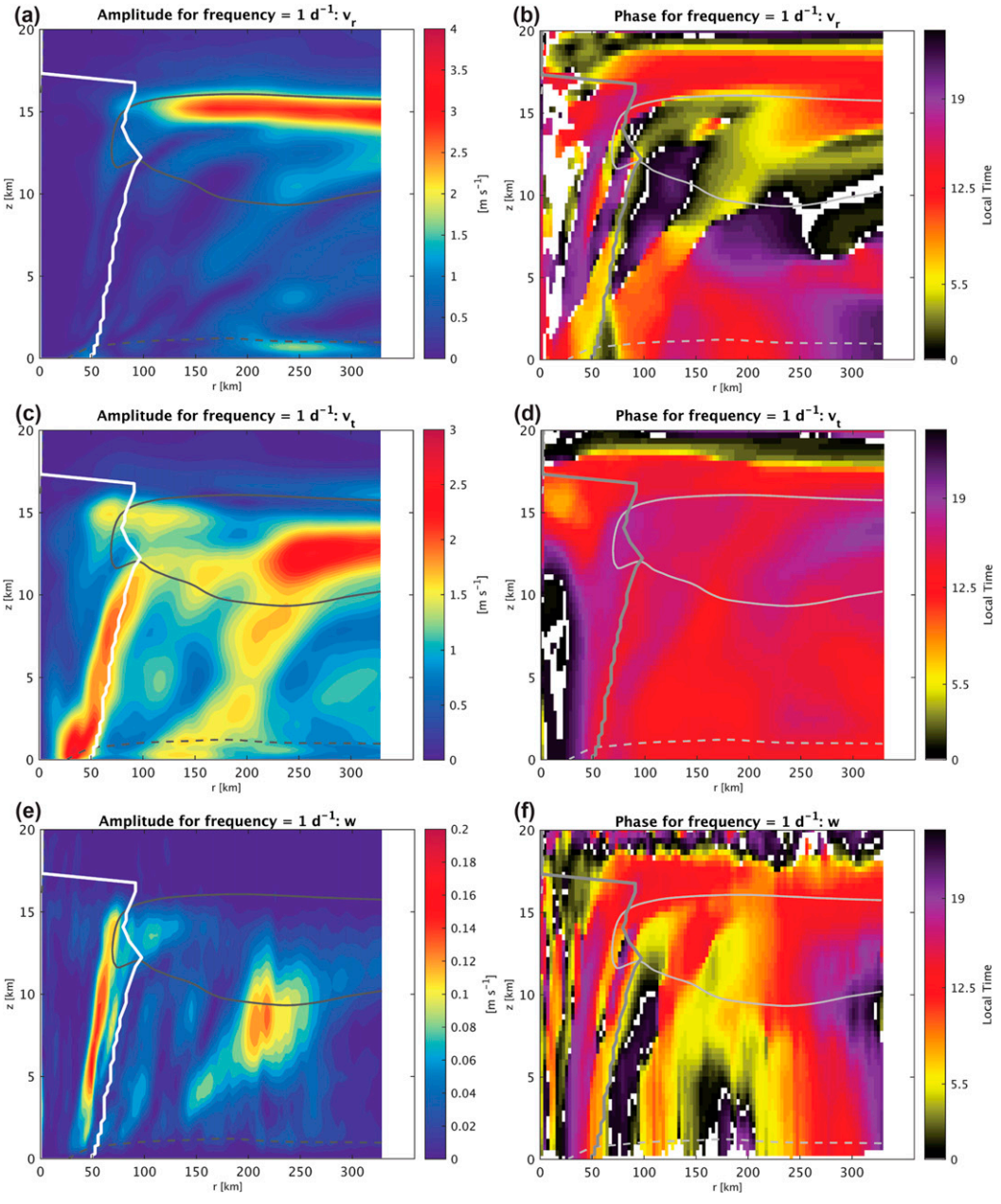

FIG. 15. (a),(c),(e) Amplitude and (b),(d),(f) phase of the diurnal cycle for the dynamics variables as a summary for HNR1: (a),(b) v_r; (c),(d) v_t; and (e),(f) w. Phase is only shown where amplitude is ≥1% of maximum amplitude. In the phase plots, the pale yellow corresponds to the average local time of sunrise in the respective simulation, the red is midday, the purple is sunset, and the black is overnight. The thin gray lines show the time mean position of the upper-level outflow (solid) and boundary layer inflow (dashed).

midday, the upper-level outflow is 4 m s^{-1} stronger, and the surface inflow is 2 m s^{-1} weaker. Overnight, the upper-level outflow is weaker, midlevel flow is anomalously outward, and surface inflow is 2 m s^{-1} stronger. In Figs. 15c and 15d, the eyewall and outflow tangential winds are 3 m s^{-1} stronger at sunset. This is coincident with the diurnal peak of eyewall convection, as shown by the positive vertical motion anomaly at sunset in the eyewall in Figs. 15e and 15f. There is also a midday peak in vertical motion in the region of the cirrus canopy, potentially providing the daytime lifting of the cirrus canopy. Additionally, there is a morning to midday peak in vertical motion from r = 150–250 km, which is likely related to the propagating squall line. In Figs. 16a and 16b, the ice mixing ratio at heights between 10 and 14 km oscillates diurnally due to the upward lifting and downward subsidence of the cirrus canopy at midday and

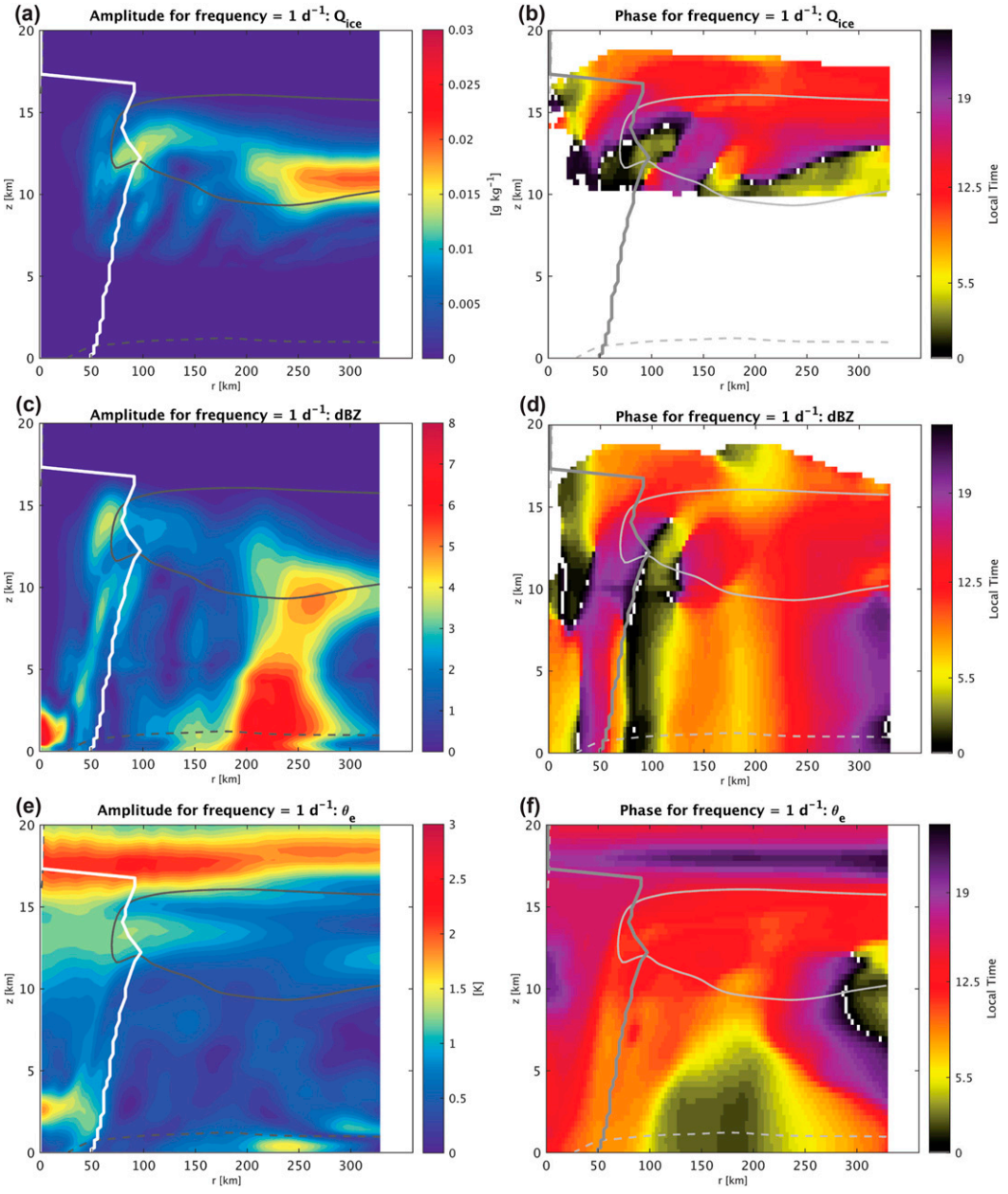

FIG. 16. (a),(c),(e) Amplitude and (b),(d),(f) phase of the diurnal cycle for some of the moisture and thermodynamic variables as a summary for HNR1: (a),(b) Q_{ice}; (c),(d) dBZ; and (e),(f) θ_e.

overnight, respectively. Just prior to sunrise, a squall line forms outside the inner core at r >160 km near sunrise as shown in Figs. 16c and 16d, and propagates outward and intensifies, reaching peak intensity at r = 200–250 km around midday, then weakening as it continues to propagate. In Figs. 16e and 16f, θ_e peaks in the lower troposphere overnight as a result of nighttime cooling and enhanced evaporation from the sea surface due to the stronger surface inflow. Solar heating of the cloud deck increases θ_e at midday in the majority of the TC, while the warm core reaches its maximum temperature at sunset coincident with the eyewall tangential wind peak in Fig. 16b due to the thermal wind relationship (Stern and Nolan 2011).

Figure 17 illustrates the diurnal cycle in the primary and secondary circulation of Florence. The magnitude and timing of changes to the circulation are largely the same as in HNR1, with some small exceptions. The Florence diurnal responses are generally much weaker than in HNR1. Furthermore, the lower-tropospheric responses are relatively weak compared to the mid- to upper tropospheric in Florence, while in HNR1 the balance between lower and upper

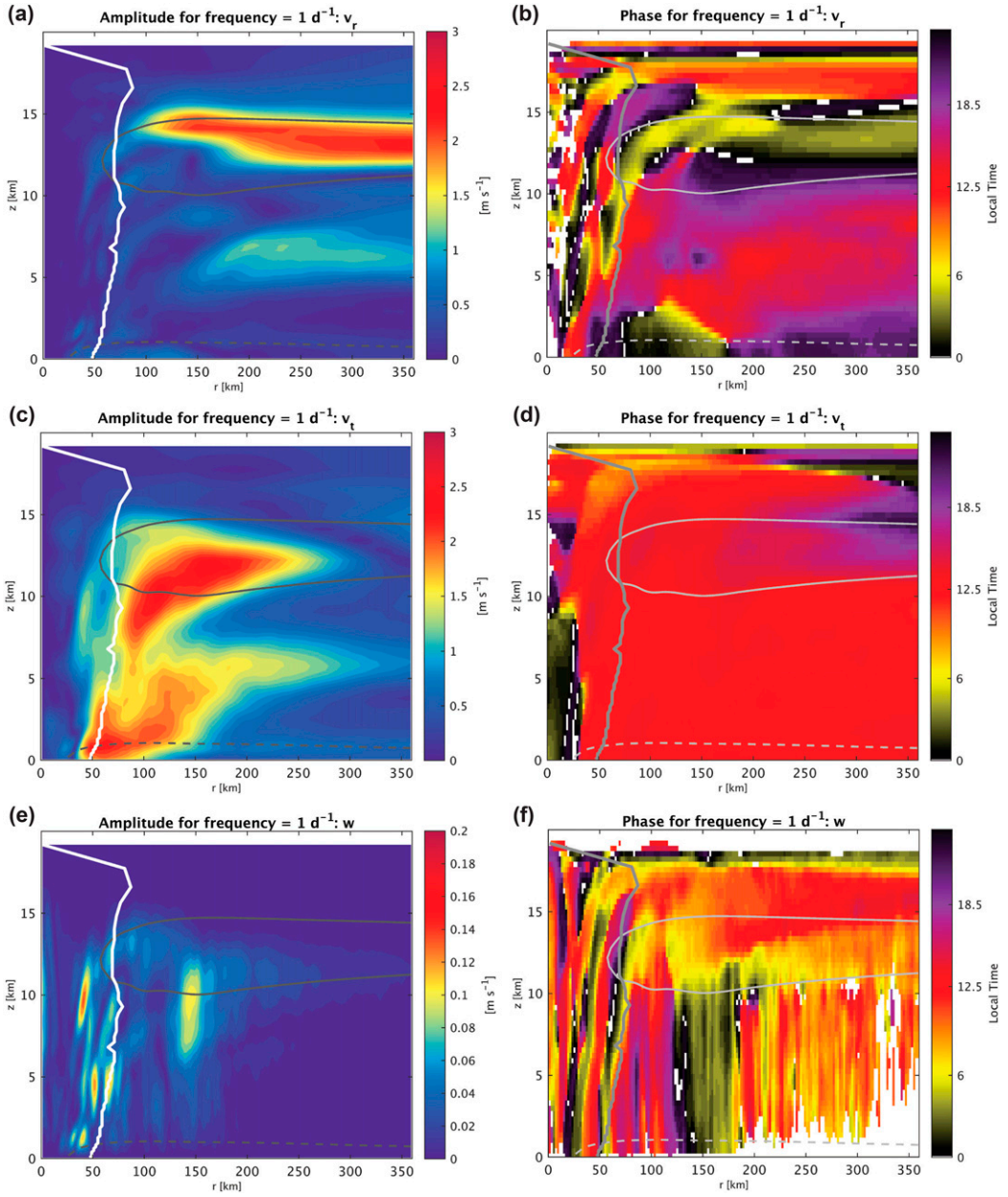

FIG. 17. (a),(c),(e) Amplitude and (b),(d),(f) phase of the diurnal cycle for the dynamics variables as a summary for Florence: (a),(b) v_r; (c),(d) v_t; and (e),(f) w.

responses are more comparable. Thus diurnal variability in Florence is skewed more toward the middle and upper levels. In Figs. 17a and 17b the upper-level outflow and anomalous midlevel inflow during the day dominate the v_r signal, with a much weaker surface inflow anomaly than in HNR1, illustrating the top-heavy nature of the Florence responses. In Figs. 17c and 17d, the outflow and inner core tangential winds peak earlier in the day than in HNR1, and the inner core tangential wind anomaly in Florence is outside the RMW. The vertical motion signal in Figs. 17e and 17f is very consistent with HNR1, with a late afternoon peak in eyewall winds, the signal associated with the propagating squall, and the daytime peak in cirrus canopy vertical motion. The upward displacement of the cirrus canopy at midday is also very consistent with HNR1 as shown in Figs. 18a and 18b. The phase plots illustrate at the ice maximum occurs at heights of 12 km and higher at midday, and at heights of 10 km overnight. The propagating squall which forms in the inner core, at $r = 125$ km near sunrise and propagates outward over the course of the day, reaching maximum intensity near midday is also consistent with HNR1 as shown in Figs. 18c and 18d.

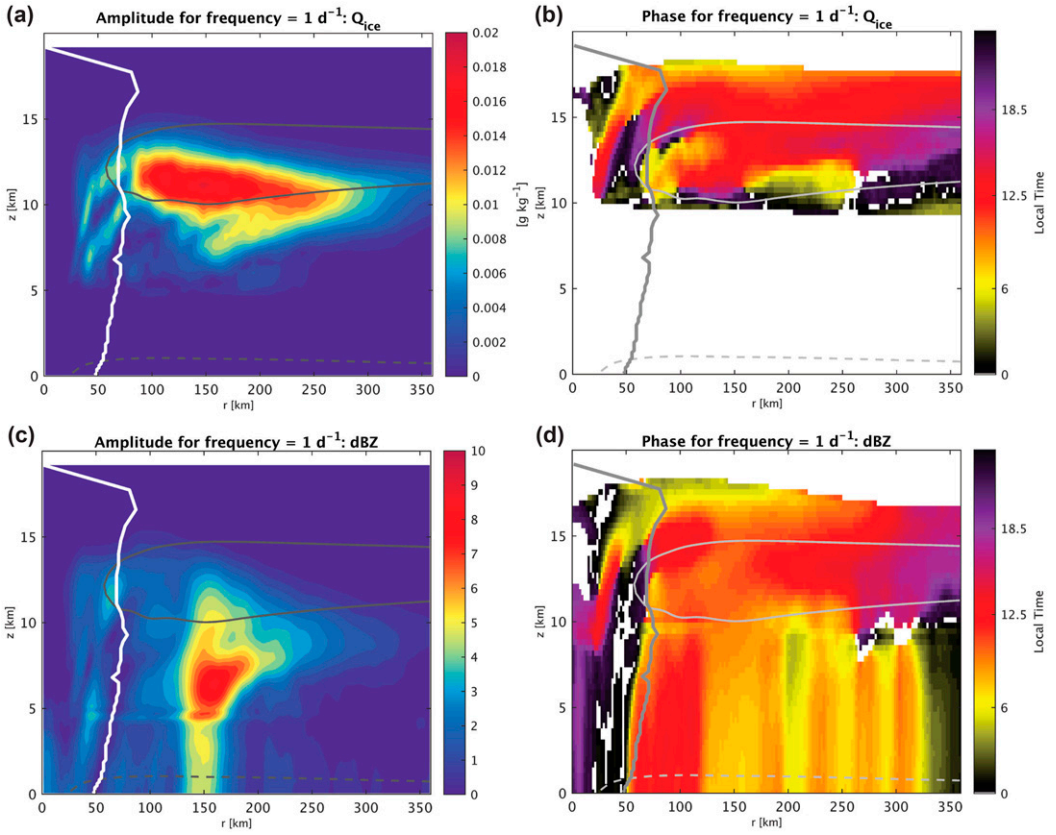

FIG. 18. (a),(c) Amplitude and (b),(d) phase of the diurnal cycle for some of the moisture and thermodynamic variables as a summary for Florence: (a),(b) Q_{ice} and (c),(d) dBZ.

4. Discussion

The results here have important implications for mechanisms by which the diurnal cycle of solar radiation manifests itself in TCs. In this section we outline some mechanisms that have been proposed in previous studies, and whether our results support or refute these ideas.

Browner et al. (1977) first noted the increase in cirrus canopy area during the day, and invoked an enhancement of the secondary circulation due to daytime differential heating between the cloudy and cloud-free regions as a mechanism. Mecikalski and Tripoli (1998) suggested that this diurnal cycle in cirrus canopy area could be related to a diurnal cycle in the inertial stability (I^2) in the outflow. To explore this mechanism, the amplitude and phase of the diurnal cycle in I^2 in HNR1 and Florence was calculated as shown in Fig. 19. The value of I^2 was calculated using $I^2 = (\partial\overline{v}/\partial r + \overline{v}/r + f)(2\overline{v}/r + f)$. As shown in Fig. 19a, the amplitude of the diurnal cycle of I^2 in HNR1 is very high in the inner core, and decreases dramatically outside the RMW. There are also signals associated with convection just outside the RMW at r = 80–140 km and z = 1–10 km, as well just inside the radius where diurnal squall forms (inside r = 150 km). There appears to be an increase in inertial stability at r = 150 km after the diurnal squall has exited this region. In the cirrus canopy in the radial range where the diurnal squall propagates (outside r = 150 km), the amplitudes of the diurnal cycle in I^2 are vanishingly small. This result is consistent between HNR1 and Florence. For this reason, it is unlikely that propagation of the diurnal squall line is heavily influenced by diurnal oscillations in inertial stability. In the outflow, the maximum amplitude of the oscillation of I^2 is extremely small and occurs at midday–sunset as shown in Figs. 19b and 19c. This is also the case in Florence, as shown in Figs. 19d–f. The amplitude of the diurnal cycle in I^2 is high in the inner core, as was the case in HNR1, with negligible amplitude in the cirrus canopy and outer radii as shown in Fig. 19c. For both HNR1 and Florence, the diurnal oscillation in I^2 in the cirrus canopy is certainly not high enough to modulate the strength of the outflow. Furthermore, as described earlier, the results presented in section 3 do not support the daytime enhancement of the outflow as the underlying mechanism behind the lifting and radial expansion of the cirrus canopy.

Dunion et al. (2014) first noted the presence of a diurnal pulse of convection that forms in the cirrus canopy inner core around sunset and propagates outward overnight. Dunion et al. (2014) cites the Mecikalski and Tripoli (1998) I^2 mechanism as a possible reason the outflow environment could become more conducive to propagation of the pulse. As shown here, the phase of the diurnal maximum of I^2 in the

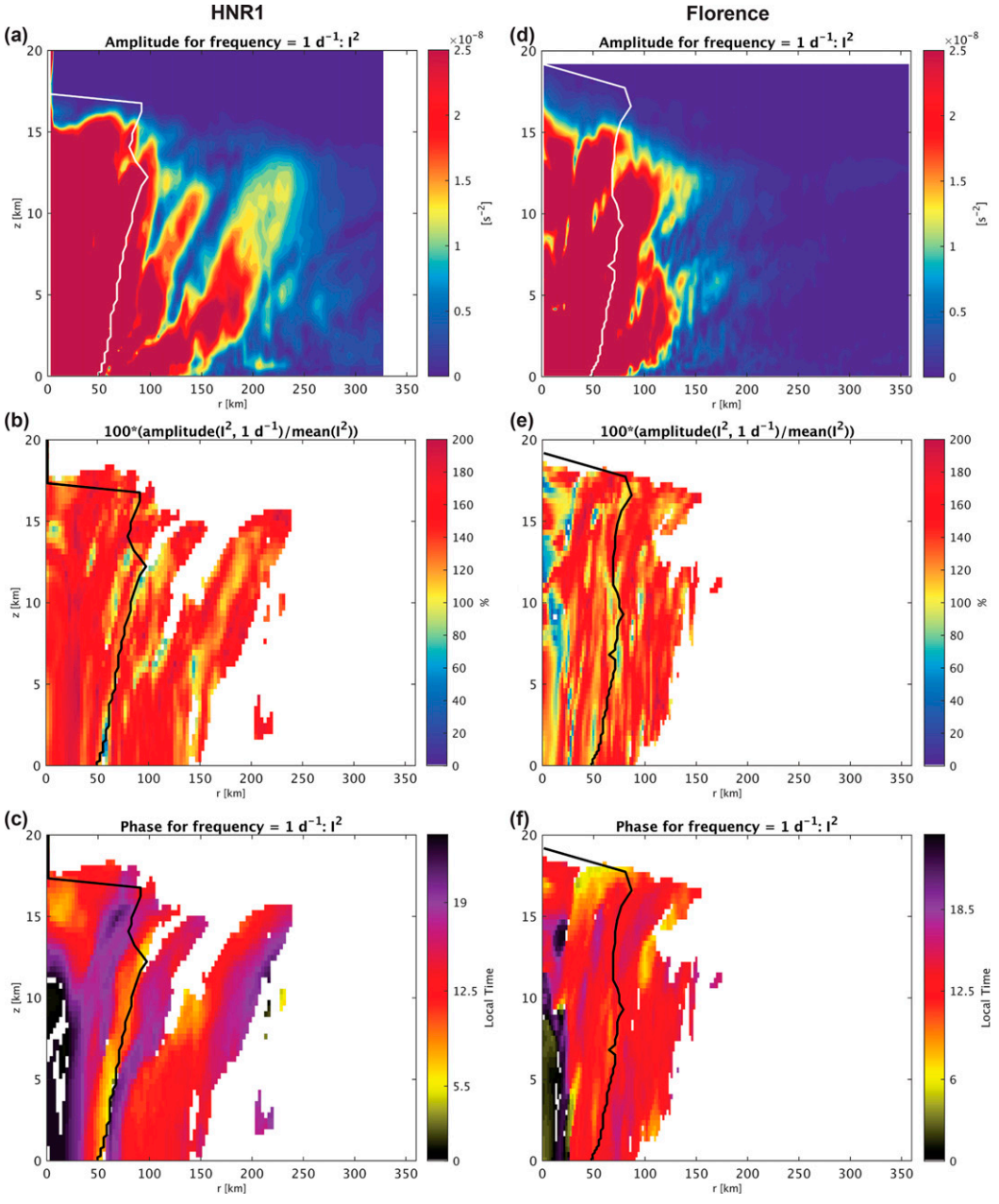

FIG. 19. (a),(b),(d),(e) Amplitude and (c),(f) phase of the diurnal cycle of I^2 in (left) HNR1 and (right) Florence. The amplitude plots are shown using (a),(d) a value of the amplitude and (b),(e) as a percentage of the time-mean value at each grid point. Plots in (a) and (d) are saturated in color scale at 2.5×10^{-8} s^{-2} to show the pattern outside the RMW in more detail. Plots in (b), (c), (e), and (f) are only shown where the amplitude of the diurnal cycle is ≥1% of the maximum amplitude.

outflow is between midday and sunset, meaning the minimum is overnight, which would in theory allow enhanced propagation of the pulse overnight. While the timing of the diurnal minimum in outflow I^2 is viable, the amplitude is not, rendering it unlikely that this mechanism is the cause of the propagation of the Dunion et al. (2014) diurnal pulse. The Mecikalski and Tripoli (1998) I^2 mechanism is unlikely to be the cause of the enhancement of upper-level outflow at midday, since (i) the amplitude is too low to allow such a dramatic diurnal cycle in v_r, and (ii) the diurnal maximum of I^2 and thus maximum theoretical restriction of radial flow is at midday, when the outflow is shown here to be at its strongest. Since the outflow is weakest at night, coincident with the propagation of the pulse, this indicates that the propagation of the pulse is not a result of advection by the background flow (i.e., it is not an advectively driven feature). Instead it is more likely that the

diurnal pulse is a trapped gravity wave or a result of the enhanced cirrus canopy convection at sunset due to the Randall et al. (1991) lapse rate mechanism.

The findings of a midday strengthening of the outflow, lifting of the cirrus canopy, and enhanced eyewall deep convection and surface inflow at sunset and overnight strongly support the findings of Ruppert and Hohenegger (2018); Ruppert and O'Neill (2019). In these studies, they invoke the Randall et al. (1991) lapse rate mechanism to explain the nighttime eyewall convective maximum. To explain the delay between the convective maximum and peak rainfall, they invoke differential cooling between the cloud versus cloud free areas, which was first proposed by Gray and Jacobson (1977) to explain the early morning maximum in tropical convection. They state that the lapse rate mechanism is the most important for the nocturnal deep convection, and the differential heating causes the rainfall peak to delay by 5 h, resulting in a rainfall peak in the early morning. Daytime upper-level solar heating is proposed to induce mesoscale upward motion in the upper levels, driving an upper-level overturning circulation during the day. Furthermore, they invoke a thermally direct lifting as the mechanism for cirrus canopy lifting, where solar heating causes anomalous vertical motion and thus the cirrus canopy to rise. Our results support these assertions, in particular that the eyewall and rainbands each exhibit their own diurnal cycle of differing phase. The results presented here support a sunset–night invigoration of eyewall convection and rainfall, and a sunrise–midday invigoration of rainband convection. This illustrates that the rainbands are more representative of the early morning maximum of tropical convection outlined in Gray and Jacobson (1977). The lifting of the cirrus canopy by anomalous vertical motion is supported by the results presented here. As shown in Fig. 15, vertical motion in the cirrus canopy is anomalously upward by around 0.05 m s^{-1} at midday. At this speed, the upward displacement of the cirrus canopy by 200–500 m would take 1–3 h. It is certainly feasible that solar heating inducing upward motion could lift the cirrus canopy the 200–500 m found here in a relatively short time scale, resulting in a cirrus canopy height maximum very soon after midday. This is effectively the same as the radiative mechanism invoked by Kossin (2002), where nocturnal cooling produces subsidence of the cirrus canopy overnight, and thereby reduction of the cirrus canopy area.

The diurnal cycle in TC rain rate has been well documented by many studies, such as Gray and Jacobson (1977), Browner et al. (1977), Randall et al. (1991), Bowman and Fowler (2015). Indeed the diurnal cycle in the amount of rain in HNR1 was found to be remarkably consistent with Bowman and Fowler (2015). They used IBTrACS and Tropical Rainfall Measuring Mission (TRMM) observations of rain in all TCs in all basins from 1998 to 2013 finding that the amplitude of the diurnal cycle of the amount of rain was 7% of the mean for any given storm. In HNR1, the diurnal cycle in the amount of rain condensate was calculated to be 6.1% of the mean, indicating that HNR1 captures the magnitude of the diurnal variability of rain with remarkable consistency. Our results indicate that the diurnal cycle in TC rain rate is dominated by a diurnal squall. Squall-like diurnal pulses in TCs have been well documented in observations (Ditchek et al. 2019a,b). Indeed, Ditchek et al. (2019b) found that these pulses were found in some capacity in 87.8% of all Atlantic TCs between 1982 and 2017. The properties of the squall-like diurnal pulses has also been studied using observations of Hurricane Harvey (2017) by Ditchek et al. (2020). The diurnal pulses in Ditchek et al. (2020) were found to have similar characteristics to tropical squalls, including outflow boundaries, a cold pool, overturning circulation, and low level jet. The formation of the squall around sunrise and the intensification as it propagates away from the inner core implies that it forms due to some mechanism for initiation like the differential cooling or lapse rate mechanisms, but only enters a favorable environment for intensification once it has propagated far enough away from the eyewall. It is possible that in the inner core moat region, the squall is suppressed by the subsiding dry air, then is able to amplify as it moves out of that region. Then later in the day when the sun sets and the column lapse rate increases, the eyewall convection can intensify uninhibited with no competition for moisture from the squall. This squall was first noted in HNR1 by Dunion et al. (2019), who postulated that there is a buildup of convective available potential energy (CAPE) overnight due to mid–upper-level radiative cooling, which preconditions the environment for squall formation in the inner core. This radiative preconditioning of the environment has been found to be important in simulations of TC genesis, by allowing humidification of the environment, promoting the onset of convection (Melhauser and Zhang 2014; Nicholls 2015). Once the environment is primed for squall formation by sunrise, the Gray and Jacobson (1977) differential heating mechanism or the Randall et al. (1991) lapse rate mechanism could result in initiation of a squall, taking advantage of the annulus of favorable CAPE that built up overnight. Since the squall is column-deep, it can then interact with the diurnal cycle in the cirrus canopy, potentially enhancing the v_t perturbation in the upper branch of the secondary circulation.

5. Conclusions

The properties of diurnal variability in TCs and the mechanisms behind them remain an elusive aspect of TC research. This study provides a comprehensive quantitative analysis of diurnal variability in two high-quality simulations of TCs to explore these mechanisms in an azimuthally averaged context. One simulation is the Nolan et al. (2013) Hurricane Nature Run (HNR1), which is a high-resolution simulation in WRF of a TC that formed in the ECMWF Joint OSSE Nature Run. The other simulation is a high-resolution simulation of Hurricane Florence (2018) in WRF using hourly ERA5 data for its boundary and initial conditions. The horizontal resolution of the domains used for analysis here are 3 and 2 km for HNR1 and Florence, respectively. Empirical orthogonal functions (EOFs) were used to analyze the modes of variability in TCs, and determine whether those modes were diurnal in nature.

Fourier analysis and filtering were used to analyze the amplitude and phase of the explicitly diurnal variability.

Overall, the two simulations presented here are very consistent with one another and previous studies using both observations and simulations. In both simulations at sunrise, a diurnal squall forms in the inner core and propagates outward, intensifying as it does so, reaching peak intensity near midday, then weakening thereafter as it continues to propagate. At midday the upper-level outflow strengthens, there is anomalous midlevel inflow, and the surface inflow is weaker. Furthermore, the TC vertically expands as the cirrus canopy displaces upward. At sunset and overnight, the surface inflow is stronger, and convection inside the RMW peaks. Therefore, three diurnal cycles of convection exist in TCs with different phases: eyewall convection at sunset and at night, rainband convection in the early morning, and the upward displacement of the cirrus canopy at midday. The diurnal cycles in rain, associated with the diurnal squall, and intensity could have implications for the forecasting of landfalling TCs. This confirms that diurnal responses are ubiquitous throughout TCs, influencing the entire dynamical, thermodynamical, and microphysical nature of the storm.

The results presented here offer insight in to some mechanisms by which the diurnal cycle of solar radiation manifests itself in TCs. We find that the diurnal cycle in inertial stability in the cirrus canopy is negligible, rendering it unlikely that diurnal variability in outflow resistance suggested by Mecikalski and Tripoli (1998) is the cause of the midday maximum in upper-level outflow, midday maximum in cirrus canopy area, or the propagation of the diurnal pulse overnight. Furthermore, this study finds that upper-level outflow is stronger at midday, and weaker at night, implying that the overnight propagation of the Dunion et al. (2014) diurnal pulse is not advectively driven. Instead it is more likely that the diurnal pulse is caused by either a gravity wave response to diurnal heating, or the lapse rate mechanism. The findings presented here of stronger upper-level outflow, weaker surface inflow, cirrus canopy lifting at midday, and enhanced eyewall deep convection at night support the findings of Ruppert and Hohenegger (2018) and Ruppert and O'Neill (2019). In their proposed mechanisms, solar heating directly lifts the cirrus canopy during the day, and produces an anomalous overturning circulation in the mid- to upper troposphere. At night, the increase in lapse rate due to upper-level radiative cooling can produce enhanced convection in the eyewall. Furthermore, this study finds that the daytime increase in the cirrus canopy area is not mechanistically linked to the enhancement of the upper-level secondary circulation, and is instead more likely to because by a direct radiative–convective interaction. Dunion et al. (2019) and Ditchek et al. (2020) suggested that radiative cooling at night could also increase CAPE overnight, preconditioning the inner core environment for the sunrise diurnal squall found in this study.

Acknowledgments. This research was supported by the National Science Foundation under Award AGS-1654831.

REFERENCES

Bowman, K. P., and M. D. Fowler, 2015: The diurnal cycle of precipitation in tropical cyclones. *J. Climate*, **28**, 5325–5334, https://doi.org/10.1175/JCLI-D-14-00804.1.

Browner, S. P., W. L. Woodley, and C. G. Griffith, 1977: Diurnal oscillation of the area of cloudiness associated with tropical storms. *Mon. Wea. Rev.*, **105**, 856–864, https://doi.org/10.1175/1520-0493(1977)105<0856:DOOTAO>2.0.CO;2.

Copernicus Climate Change Service (C3S), 2017: ERA5: Fifth generation of ECMWF atmospheric reanalyses of the global climate. Copernicus Climate Change Service Climate data store (CDS), accessed 24 February 2020, https://cds.climate.copernicus.eu/cdsapp#!/home.

Ditchek, S. D., K. L. Corbosiero, R. G. Fovell, and J. Molinari, 2019a: Electrically active tropical cyclone diurnal pulses in the Atlantic basin. *Mon. Wea. Rev.*, **147**, 3595–3607, https://doi.org/10.1175/MWR-D-19-0129.1.

——, J. Molinari, K. L. Corbosiero, and R. G. Fovell, 2019b: An objective climatology of tropical cyclone diurnal pulses in the Atlantic basin. *Mon. Wea. Rev.*, **147**, 591–605, https://doi.org/10.1175/MWR-D-18-0368.1.

——, K. L. Corbosiero, R. G. Fovell, and J. Molinari, 2020: Electrically active diurnal pulses in Hurricane Harvey (2017). *Mon. Wea. Rev.*, **148**, 2283–2305, https://doi.org/10.1175/MWR-D-20-0022.1.

Dunion, J. P., C. D. Thorncroft, and C. S. Velden, 2014: The tropical cyclone diurnal cycle of mature hurricanes. *Mon. Wea. Rev.*, **142**, 3900–3919, https://doi.org/10.1175/MWR-D-13-00191.1.

——, ——, and D. S. Nolan, 2019: Tropical cyclone diurnal cycle signals in a hurricane nature run. *Mon. Wea. Rev.*, **147**, 363–388, https://doi.org/10.1175/MWR-D-18-0130.1.

Evans, R. C., and D. S. Nolan, 2019: Balanced and radiating wave responses to diurnal heating in tropical cyclone–like vortices using a linear nonhydrostatic model. *J. Atmos. Sci.*, **76**, 2575–2597, https://doi.org/10.1175/JAS-D-18-0361.1.

Gray, W. M., and R. W. Jacobson, 1977: Diurnal variation of deep cumulus convection. *Mon. Wea. Rev.*, **105**, 1171–1188, https://doi.org/10.1175/1520-0493(1977)105<1171:DVODCC>2.0.CO;2.

Iacono, M. J., J. S. Delamere, E. J. Mlawer, M. W. Shephard, S. A. Clough, and W. D. Collins, 2008: Radiative forcing by long-lived greenhouse gases: Calculations with the AER radiative transfer models. *J. Geophys. Res.*, **113**, D13103, https://doi.org/10.1029/2008JD009944.

Kain, J. S., 2004: The Kain–Fritsch convective parameterization: An update. *J. Appl. Meteor.*, **43**, 170–181, https://doi.org/10.1175/1520-0450(2004)043<0170:TKCPAU>2.0.CO;2.

Knaff, J. A., C. J. Slocum, and K. D. Musgrave, 2019: Quantification and exploration of diurnal oscillations in tropical cyclones. *Mon. Wea. Rev.*, **147**, 2105–2121, https://doi.org/10.1175/MWR-D-18-0379.1.

Kossin, J. P., 2002: Daily hurricane variability inferred from GOES infrared imagery. *Mon. Wea. Rev.*, **130**, 2260–2270, https://doi.org/10.1175/1520-0493(2002)130<2260:DHVIFG>2.0.CO;2.

Lim, K.-S. S., and S.-Y. Hong, 2010: Development of an effective double-moment cloud microphysics scheme with prognostic cloud condensation nuclei (CCN) for weather and climate models. *Mon. Wea. Rev.*, **138**, 1587–1612, https://doi.org/10.1175/2009MWR2968.1.

Mecikalski, J. R., and G. J. Tripoli, 1998: Inertial available kinetic energy and the dynamics of tropical plume formation. *Mon. Wea. Rev.*, **126**, 2200–2216, https://doi.org/10.1175/1520-0493(1998)126<2200:IAKEAT>2.0.CO;2.

Melhauser, C., and F. Zhang, 2014: Diurnal radiation cycle impact on the pregenesis environment of Hurricane Karl (2010). *J. Atmos. Sci.*, **71**, 1241–1259, https://doi.org/10.1175/JAS-D-13-0116.1.

Morrison, H., G. Thompson, and V. Tatarskii, 2009: Impact of cloud microphysics on the development of trailing stratiform precipitation in a simulated squall line: Comparison of one- and two-moment schemes. *Mon. Wea. Rev.*, **137**, 991–1007, https://doi.org/10.1175/2008MWR2556.1.

Muramatsu, T., 1983: Diurnal variations of satellite-measured TBB areal distribution and eye diameter of mature typhoons. *J. Meteor. Soc. Japan*, **61**, 77–90, https://doi.org/10.2151/jmsj1965.61.1_77.

Navarro, E. L., and G. J. Hakim, 2016: Idealized numerical modeling of the diurnal cycle of tropical cyclones. *J. Atmos. Sci.*, **73**, 4189–4201, https://doi.org/10.1175/JAS-D-15-0349.1.

——, ——, and H. E. Willoughby, 2017: Balanced response of an axisymmetric tropical cyclone to periodic diurnal heating. *J. Atmos. Sci.*, **74**, 3325–3337, https://doi.org/10.1175/JAS-D-16-0279.1.

Nicholls, M. E., 2015: An investigation of how radiation may cause accelerated rates of tropical cyclogenesis and diurnal cycles of convective activity. *Atmos. Chem. Phys.*, **15**, 9003–9029, https://doi.org/10.5194/acp-15-9003-2015.

Nolan, D. S., R. Atlas, K. T. Bhatia, and L. R. Bucci, 2013: Development and validation of a hurricane nature run using the joint OSSE nature run and the WRF model. *J. Adv. Model. Earth Syst.*, **5**, 382–405, https://doi.org/10.1002/jame.20031.

O'Neill, M. E., D. Perez-Betancourt, and A. A. Wing, 2017: Accessible environments for diurnal-period waves in simulated tropical cyclones. *J. Atmos. Sci.*, **74**, 2489–2502, https://doi.org/10.1175/JAS-D-16-0294.1.

Randall, D. A., Harshvardhan, and D. A. Dazlich, 1991: Diurnal variability of the hydrologic cycle in a general circulation model. *J. Atmos. Sci.*, **48**, 40–62, https://doi.org/10.1175/1520-0469(1991)048<0040:DVOTHC>2.0.CO;2.

Ruppert, J. H., and C. Hohenegger, 2018: Diurnal circulation adjustment and organized deep convection. *J. Climate*, **31**, 4899–4916, https://doi.org/10.1175/JCLI-D-17-0693.1.

——, and M. E. O'Neill, 2019: Diurnal cloud and circulation changes in simulated tropical cyclones. *Geophys. Res. Lett.*, **46**, 502–511, https://doi.org/10.1029/2018GL081302.

Schmit, T. J., S. S. Lindstrom, J. J. Gerth, and M. M. Gunshor, 2018: Applications of the 16 spectral bands on the advanced baseline imager. *J. Oper. Meteor.*, **6**, 33–46, https://doi.org/10.15191/nwajom.2018.0604.

Stern, D. P., and D. S. Nolan, 2011: On the vertical decay rate of the maximum tangential winds in tropical cyclones. *J. Atmos. Sci.*, **68**, 2073–2094, https://doi.org/10.1175/2011JAS3682.1.

Stewart, S. R., and R. Berg, 2019: Tropical cyclone report: Hurricane Florence (31 August–17 September 2018). Tech. Rep. AL062018, National Hurricane Center, 98 pp., https://www.nhc.noaa.gov/data/tcr/AL062018_Florence.pdf.

Tang, X., and F. Zhang, 2016: Impacts of the diurnal radiation cycle on the formation, intensity, and structure of Hurricane Edouard (2014). *J. Atmos. Sci.*, **73**, 2871–2892, https://doi.org/10.1175/JAS-D-15-0283.1.

——, Z.-M. Tan, J. Fang, Y. Q. Sun, and F. Zhang, 2017: Impact of the diurnal radiation cycle on secondary eyewall formation. *J. Atmos. Sci.*, **74**, 3079–3098, https://doi.org/10.1175/JAS-D-17-0020.1.

——, ——, ——, E. B. Munsell, and F. Zhang, 2019: Impact of the diurnal radiation contrast on the contraction of radius of maximum wind during intensification of Hurricane Edouard (2014). *J. Atmos. Sci.*, **76**, 421–432, https://doi.org/10.1175/JAS-D-18-0131.1.

Tripoli, G. J., and W. R. Cotton, 1989: Numerical study of an observed orogenic mesoscale convective system. Part I: Simulated genesis and comparison with observations. *Mon. Wea. Rev.*, **117**, 273–304, https://doi.org/10.1175/1520-0493(1989)117<0273:NSOAOO>2.0.CO;2.

Zhang, C., and Y. Wang, 2017: Projected future changes of tropical cyclone activity over the western North and South Pacific in a 20-km-mesh regional climate model. *J. Climate*, **30**, 5923–5941, https://doi.org/10.1175/JCLI-D-16-0597.1.

Zhang, J. A., J. P. Dunion, and D. S. Nolan, 2020: In-situ observations of the diurnal variation in the boundary layer of mature hurricanes. *Geophys. Res. Lett.*, **47**, 2019GL086206, https://doi.org/10.1029/2019GL086206.